Assimilation of Z_{DR} Columns for Improving the Spinup and Forecast of Convective Storms in Storm-Scale Models: Proof-of-Concept Experiments

JACOB T. CARLIN

School of Meteorology, and Cooperative Institute for Mesoscale Meteorological Studies, University of Oklahoma, and NOAA/OAR/National Severe Storms Laboratory, Norman, Oklahoma

JIDONG GAO

NOAA/OAR/National Severe Storms Laboratory, Norman, Oklahoma

JEFFREY C. SNYDER AND ALEXANDER V. RYZHKOV

Cooperative Institute for Mesoscale Meteorological Studies, University of Oklahoma, and NOAA/OAR/National Severe Storms Laboratory, Norman, Oklahoma

(Manuscript received 18 April 2017, in final form 21 September 2017)

ABSTRACT

Achieving accurate storm-scale analyses and reducing the spinup time of modeled convection is a primary motivation for the assimilation of radar reflectivity data. One common technique of reflectivity data assimilation is using a cloud analysis, which inserts temperature and moisture increments and hydrometeors deduced from radar reflectivity via empirical relations to induce and sustain updraft circulations. Polarimetric radar data have the ability to provide enhanced insight into the microphysical and dynamic structure of convection. Thus far, however, relatively little has been done to leverage these data for numerical weather prediction. In this study, the Advanced Regional Prediction System's cloud analysis is modified from its original reflectivity-based formulation to provide moisture and latent heat adjustments based on the detection of differential reflectivity columns, which can serve as proxies for updrafts in deep moist convection and, subsequently, areas of saturation and latent heat release. Cycled model runs using both the original cloud analysis and above modifications are performed for two high-impact weather cases: the 19 May 2013 central Oklahoma tornadic supercells and the 25 May 2016 north-central Kansas tornadic supercell. The analyses and forecasts of convection qualitatively and quantitatively improve in both cases, including more coherent analyzed updrafts, more realistic forecast reflectivity structures, a better correspondence between forecast updraft helicity tracks and radar-derived rotation tracks, and improved frequency biases and equitable threat scores for reflectivity. Based on these encouraging results, further exploration of the assimilation of dual-polarization radar data into storm-scale models is warranted.

1. Introduction

The assimilation of radar data into convective-scale numerical weather prediction (NWP) models has gained considerable attention in recent years with increased operational implementation and use in the warning decision process (e.g., the ''Warn-on-Forecast'' initiative; Stensrud et al. 2009, 2013). Weather radar is one of the only sources of data available that provides information at a temporal and spatial resolution comparable to convection-allowing NWP models. Thus, radar data assimilation's ability to promote deep moist convection and its attendant perturbations in NWP models and to reduce the spinup time has been and continues to be explored. However, most efforts to date have been limited to measurements of reflectivity at horizontal polarization (hereafter, Z) and radial velocity.

Many methods of assimilating Z have been studied over the past two decades. One of the earliest methods examined was four-dimensional variational data assimilation (4DVAR), which uses the forecast model as a dynamical constraint during the assimilation process. While results have been encouraging (e.g., Sun and Crook 1997, 1998; Sun 2005; Sun and Zhang 2008; Wang et al. 2013b), the difficulty of developing and maintaining an adjoint model and the inherent nonlinearities of the microphysics scheme

Corresponding author: Jacob T. Carlin, jacob.carlin@noaa.gov

DOI: 10.1175/MWR-D-17-0103.1

often hinder proper convergence of the cost function. As such, 4DVAR methods have not been widely used for convective-scale radar data assimilation and have typically been limited to warm rain microphysics, although recent work has begun to investigate the inclusion of some ice phases (Chang et al. 2016). The simpler and more computationally efficient three-dimensional variational data assimilation (3DVAR) method has provided positive results (e.g., Xiao et al. 2005, 2007; Gao and Stensrud 2012; Wang et al. 2013a). However, 3DVAR lacks flow-dependent error covariances, which may limit the ability to update unobserved variables, and requires limiting assumptions about the model microphysics. In recent years, the ensemble Kalman filter method (EnKF; Evensen 1994) has become increasingly popular for convective-scale radar data assimilation with very promising results for producing accurate storm-scale analyses (e.g., Dowell et al. 2004, 2011; Tong and Xue 2005; Xue et al. 2006; Aksoy et al. 2009; Yussouf and Stensrud 2010; Snook et al. 2011, 2012; Yussouf et al. 2013; Wheatley et al. 2015). However, ensemble methods are computationally expensive, may suffer from issues related to rank deficiency (e.g., filter divergence due to sampling errors; Gao et al. 2014), and have not yet seen widespread operational implementation. Hybrid methods combining the strengths of variational and ensemble methods by defining ensemble-derived flow-dependent covariances for the variational scheme are being developed (e.g., Wang et al. 2008a,b) and investigated for use with radar data assimilation at the convective scale (e.g., Gao et al. 2013, 2016; Gao and Stensrud 2014).

Other assimilation techniques assimilate state variables indirectly retrieved from Z. These methods include latent heating nudging (e.g., Jones and Macpherson 1997; Macpherson 2001; Leuenberger and Rossa 2007; Stephan et al. 2008), specific humidity nudging (Davolio and Buzzi 2004), and divergence nudging (Korsholm et al. 2015), as well as techniques that use regions of observed Z to activate a convective parameterization scheme (Rogers et al. 2000) or variationally assimilate retrieved relative humidity profiles (Caumont et al. 2010). One of the most prominent methods is the Advanced Regional Prediction System's (ARPS) cloud analysis (hereafter "cloud analysis"; Zhang et al. 1998; Zhang 1999; Brewster 2002; Hu et al. 2006a). The cloud analysis is based on the Local Analysis Prediction System (Albers et al. 1996) and makes adjustments to the model relative humidity, hydrometeor mixing ratios, and temperature based on radar, satellite, and surface observation data. Cloud analysis techniques are conceptually straightforward, computationally efficient, and have been shown to be useful for reducing the spinup of observed storms and improving short-term convective forecasts (e.g., Xue et al. 2003, 2014; Souto et al. 2003; Dawson and Xue 2006; Hu et al. 2006a; Zhao and Xue 2009; Schenkman et al. 2011; Dawson et al. 2015; Zhuang et al. 2016). Benefits can be amplified when the cloud analysis is used in conjunction with radial velocity information. To update multiple unobserved model variables from Z alone, however, cloud analysis techniques rely on semiempirical quantitative relations (e.g., retrieving hydrometeor mixing ratios from Z) and general rules relating Z to the aforementioned variables (e.g., saturating regions within a given Z threshold). These relations and rules require simplifications that can introduce errors (e.g., Gao et al. 2009; Carlin et al. 2016).

The operational WSR-88D network in the United States has been upgraded to dual-polarization, with other countries, including Germany, Canada, and the United Kingdom, following suit. These networks now provide an unprecedented volume of polarimetric observations. In contrast to single-polarization radars, dual-polarization radars transmit and receive orthogonally polarized electromagnetic waves from which information about a target's size, shape, orientation, and composition can be garnered (e.g., Kumjian 2013a). In addition to Z, measured variables include differential reflectivity Z_{DR}, copolar correlation coefficient ρ_{hv}, and differential phase shift Φ_{DP}. Dual-polarization radar data have been successfully leveraged to improve attenuation correction (e.g., Bringi et al. 1990; Testud et al. 2000; Snyder et al. 2010), quantitative precipitation estimation (e.g., Zrnić and Ryzhkov 1996; Ryzhkov et al. 2005a; Tabary et al. 2011), hydrometeor classification (e.g., Park et al. 2009), tornado detection (e.g., Ryzhkov et al. 2005b; Schultz et al. 2012a,b; Bodine et al. 2013, 2014; Van Den Broeke and Jauernic 2014; Snyder and Ryzhkov 2015), and the identification (e.g., Heinselman and Ryzhkov 2006) and size discrimination (e.g., Ryzhkov et al. 2013a,b) of hail. For further review of weather radar polarimetry, see Zrnić and Ryzhkov (1999), Bringi and Chandrasekar (2001), and Kumjian (2013a,b,c).

In recent years, numerous distinct polarimetric "signatures" have been identified and tied to dynamical and microphysical processes within storms. One of the most ubiquitous polarimetric signatures observed in deep moist convection is the Z_{DR} column. Differential reflectivity columns are vertical protrusions of positive Z_{DR} above the environmental 0°C level and are indicative of wet ice particles and oblate, supercooled raindrops in the process of freezing being lofted by the updraft. Values of Z_{DR} within these columns can exceed 4 dB at S band (radar wavelengths of approximately 10 cm) and can reach beyond 3 km above the 0°C level in extreme cases (Kumjian et al. 2014; Snyder et al. 2015). Because Z_{DR} columns are associated with convective

storm updrafts, they can theoretically be used as identifiers for regions of positive temperature perturbations from latent heat release due to condensation and/or freezing. Although the connection between Z_{DR} columns and updraft *location* has been long known (e.g., Hall et al. 1984; Illingworth et al. 1987; Tuttle et al. 1989; Ryzhkov et al. 1994), recent work has begun to investigate the relationship between Z_{DR} columns and updraft *intensity*. Simulations in Kumjian et al. (2014) showed a relationship between Z_{DR} column depth (i.e., the distance above the 0°C level that enhanced values of Z_{DR} extend within the column) and updraft strength. Both Picca et al. (2010) and Kumjian et al. (2014) showed a correlation between Z_{DR} column height and hail mass at the surface at appreciable lag times, which has the potential to provide increased lead time for forecasting hail at the surface as compared to traditional metrics such as 20-dBZ echo-top height.

In addition to the aforementioned Z_{DR} columns associated with mature updrafts, enhanced Z_{DR} coincident with low values of Z has been observed aloft in the nascent stages of developing convection (e.g., Illingworth et al. 1987; Knight 2006) due to the rapid size sorting of initial precipitation particles (Picca et al. 2017). While technically distinct from Z_{DR} columns, these bursts of enhanced Z_{DR} aloft in the updraft may prove useful for identifying developing updrafts. For the sake of simplicity, both of these phenomena will be referred to as "Z_{DR} columns." For a more complete review of Z_{DR} columns, see Kumjian et al. (2014) and Snyder et al. (2015).

Despite the connection between dual-polarization radar and the microphysical and thermodynamic characteristics of deep moist convection, leveraging polarimetric data for NWP is a relatively new area of research. Predicated on the idea that a physically accurate microphysics scheme should be able to reproduce realistic polarimetric signatures, many studies have explored the use of polarimetric radar forward operators (e.g., Jung et al. 2008a, 2010a; Pfeifer et al. 2008; Ryzhkov et al. 2011) to evaluate the performance of microphysics schemes (e.g., Jung et al. 2008a, 2010a, 2012; Ryzhkov et al. 2011, 2013a; Kumjian and Ryzhkov 2012; Dawson et al. 2013, 2014; Kumjian et al. 2014; Putnam et al. 2014; Johnson et al. 2016; Snyder et al. 2017a,b). If large discrepancies are present between the model-derived polarimetric signatures and those observed in nature, it can be indicative of deficiencies in the microphysics scheme. Alternatively, if a model faithfully reproduces polarimetric signatures as they are observed in nature, the model can be used to investigate what physical processes are responsible for a given signature. Some studies have used polarimetric data to assimilate improved estimates of rainwater mixing ratio using both 3DVAR (Li and Mecikalski 2010, 2012) and EnKF (Yokota et al. 2016) methods and found positive impacts compared to experiments that assimilated mixing ratios retrieved from Z alone. However, ice phases were neglected. Wu et al. (2000) attempted to use Z_{DR} to differentiate between liquid and ice phases for hydrometeor mass retrievals using 4DVAR but found little success attributed to inadequate model physics. Few studies have attempted to directly assimilate polarimetric data. Using an EnKF framework, simulated polarimetric data were assimilated in addition to Z to estimate state variables (Jung et al. 2008a,b) and microphysical parameters (Jung et al. 2010b), with positive impacts found in both cases. Assimilating observed polarimetric data remains difficult because of data quality concerns and uncertainties in polarimetric operators.

This study explores the impact of assimilating observed polarimetric data through a modified cloud analysis routine. The cloud analysis technique was chosen because of its proven success in reducing spinup time and ease of implementation into existing code infrastructure. Direct insertion of the retrieved temperature and moisture perturbations is currently more straightforward than assimilating the polarimetric variables using variational techniques, which require cross covariances between model state variables and the polarimetric variables that are not currently well formulated. Section 2 details the modifications made to the existing cloud analysis routine, and section 3 describes the experimental setup used in this study. Results are presented in section 4, followed by a summary and discussion in section 5.

2. Description of data assimilation routine

a. *ARPS 3DVAR routine*

The first step of the assimilation cycling procedure makes use of the ARPS 3DVAR routine (Gao et al. 2004; Hu et al. 2006b). ARPS 3DVAR minimizes a cost function with a recursive filter containing terms for the background and observations as well as an anelastic mass continuity term as a weak constraint to produce a more balanced three-dimensional analysis of the model state variables from multiple data sources. The system is designed to work with a number of observation types including surface and upper-air observations and radial velocity. As it was designed for use at the storm scale, the routine includes multiple analysis passes with varying scales of spatial influence to help resolve flows at different scales. The resultant analysis is then used as the background when invoking the cloud analysis routine.

b. Existing cloud analysis

In the current cloud analysis, the radar data are first quality controlled and interpolated to the model grid (Brewster et al. 2005; Brewster and Stratman 2015). The process for the polarimetric variables follows that of radial velocity and Z. Radar data at ranges between 3 and 230 km from the radar site are processed. Anomalous propagation is removed using gradients and texture fields of Z and low wind speeds, with additional filtering of nonmeteorological echoes using a user-defined ρ_{hv} threshold (default of 0.85 for S band). All variables are smoothed using a nine-point median filter. Specific differential phase shift K_{DP} is calculated from Φ_{DP} from a local least squares fit on smoothed data using a Z-dependent averaging window. Remapping to the model grid of all radar variables is performed using a least squares fit to a local polynomial function, which thins the data near the radar and interpolates it at distances far from the radar (Brewster et al. 2005). For the latest changes to the cloud analysis, see Brewster and Stratman (2015).

An initial cloud fraction field is diagnosed from the background relative humidity field following a similar approach as Koch et al. (1997). Subsequently, clouds are directly inserted by setting the cloud fraction to 100% above the surface-based lifted condensation level anywhere Z exceeds a threshold, set to 15 dBZ above 2 km by default. Cloud water and ice content can be determined either adiabatically or, as in this case, using the Smith–Feddes model (Haines et al. 1989) with a reduction for entrainment following Hu et al. (2006a). Next, the dominant hydrometeor species in each grid box is determined using temperature and Z thresholds, where snow (rain) is considered when the temperature is below (above) 0°C, and where hail is considered when the Z exceeds 45 dBZ (Albers et al. 1996; Pan et al. 2016). In the case of cycling, the species can also be determined by the existing species in the model background. The mixing ratios of each species are then typically retrieved using single-moment retrieval equations for rain, snow, and hail based on Smith et al. (1975) and Lin et al. (1983). Summaries of these equations can be found in Dowell et al. (2011), Carlin et al. (2016), and Pan et al. (2016). However, recent work has initialized intercept parameters (and, if needed, shape parameters) for multimoment microphysics schemes using iterative techniques (Brewster and Stratman 2015), while other studies have found positive impacts from using single-moment microphysics schemes with intercept parameters diagnosed from hydrometeor mixing ratios (e.g., Wainwright et al. 2014; Pan et al. 2016), as developed in Zhang et al. (2008).

A temperature adjustment is then made to account for latent heat release. This can be done by simply adding the latent heating associated with the added cloud water and ice content (Zhang et al. 1998) or by assuming a moist-adiabatic temperature profile from cloud base with entrainment effects included (Brewster 2002). In this study, the latter method is applied to regions with vertical velocity $w > -0.2\ \mathrm{m\,s^{-1}}$ (determined from the 3DVAR analysis) with a linear ramp from no heating to full heating between $w = -0.2$ and $0.0\ \mathrm{m\,s^{-1}}$. Final moisture adjustments are made by reestablishing saturation anywhere the Z threshold for clouds is exceeded (incorporating the previously made temperature adjustment) or to 95% anywhere the analyzed hydrometeor mass is less than the background hydrometeor mass to help avoid overmoistening. Further details of the cloud analysis and its latest updates can be found in Brewster and Stratman (2015) and Tong (2015).

c. Modified cloud analysis

The modifications made to the cloud analysis in this study involve the final two steps of moistening and heating in updraft areas. Many studies have shown that both temperature perturbations (e.g., Hu et al. 2006a) and the initial moisture field (e.g., Weygandt et al. 2002; Ge et al. 2013) can play primary roles in determining the accuracy of modeled convection. The insertion of too much water vapor can result in an overestimate of the intensity and areal coverage of convection, leading to a degradation of the forecast (e.g., Schenkman et al. 2011; Schenkman 2012). This issue was examined in detail in Tong (2015), who found that saturating based on a Z threshold can result in too much moisture being added and large degradations in forecast skill. Forecast skill was greatly improved when a more accurate initial moisture field was provided in an observing system simulation experiment. Because of the lack of a direct relationship between in-cloud moisture and conventional observations, Tong (2015) proposed a modification to the cloud analysis in which the relative humidity in downdraft regions, which are generally unsaturated, is reduced. Notable improvements were found for both the analysis and forecast for all state variables examined, further highlighting the importance of improving the initial moisture field for convective storm-scale modeling. Despite these encouraging results, certain issues remain. While unsaturated regions correspond well with downdrafts overall, the specific quantitative relationship between water vapor mixing ratio q_v and w is unknown and poorly constrained. In addition, even with a perfect q_v–w relationship, the success of this method relies on an accurate model analysis of w, which is not always known and/or guaranteed, particularly when few radars

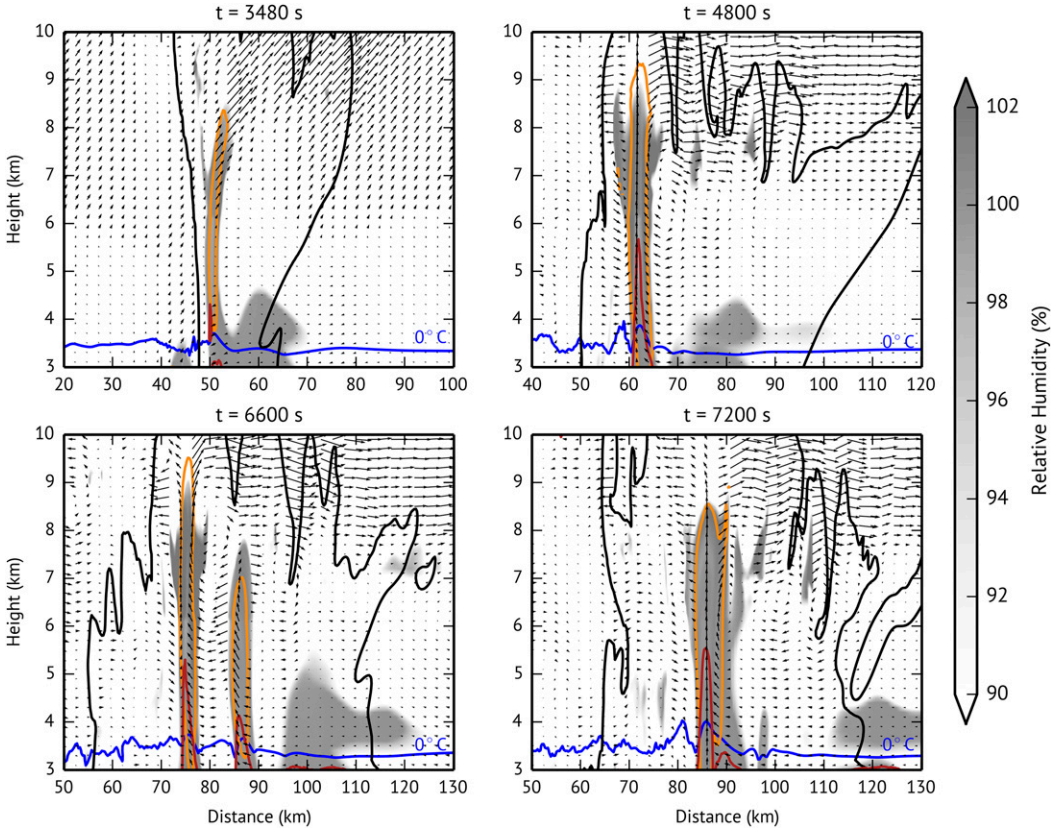

FIG. 1. Vertical cross sections of simulated deep moist convection from the Hebrew University Cloud Model showing relative humidity (shaded gray above 90%), the 100 K h^{-1} latent heating rate contour (orange), the 1.0-dB Z_{DR} contour (red), the 15-dBZ Z contour (black), the environmental 0°C level (blue), and storm-relative wind vectors in the x–z plane (arrows).

are available for assimilation. As an alternative to using w, a method is proposed using Z_{DR} columns to provide adjustments to temperature and moisture in the cloud analysis similar to the methods for assimilating lightning data at the cloud scale put forth by Fierro et al. (2012, 2014, 2015) and Marchand and Fuelberg (2014).

To investigate the validity of the proposed modifications, vertical cross sections of relative humidity, latent heating rate, Z_{DR}, Z, and storm-relative winds from a convective storm simulated by the Hebrew University Cloud Model (HUCM) are shown in Fig. 1. The HUCM is a two-dimensional nonhydrostatic cloud model with spectral bin microphysics (Khain et al. 2004). The model is coupled to a sophisticated polarimetric radar operator (Ryzhkov et al. 2011)—at S band in this case—that has been shown to recreate realistic polarimetric signatures in deep moist convection (e.g., Ryzhkov et al. 2013a; Kumjian et al. 2014; Snyder et al. 2015). The simulation shown in Fig. 1 was initialized with a sounding from a damaging hailstorm that struck Germany in 2006 (Noppel et al. 2010) and run with a 100-m vertical and 300-m horizontal grid spacing. The initial low-level cloud condensation nuclei concentration was 3000 cm^{-3}, representing polluted conditions. Throughout the lifetime of the storm, the Z_{DR} columns are coincident with updrafts featuring deep plumes of saturation and with the region of latent heating directly above the columns. Notably, the area contained within the 15-dBZ contour is much more extensive than the areas that are near or at saturation, with large regions exhibiting subsaturation. It is clear that saturating everywhere within the 15-dBZ threshold would result in too much moisture being added to the system, possibly inhibiting the formation of evaporation- or sublimation-driven downdrafts. These results support the conceptual model of Z_{DR} columns and their use as proxies for updrafts and subsequently areas of moistening and heating. It should be noted, however, that while 15 dBZ is the default threshold for saturation in the cloud analysis, it is an adjustable parameter and there is no agreed-upon Z threshold to use. Other studies have addressed overmoistening concerns by instead reducing the frequency of applications of moistening (e.g., Schenkman et al. 2011).

In this study, polarimetric data are first quality controlled and mapped to the model grid as described in section 2b. Areas of interest are limited to regions in which $Z \geq 10$ dBZ and $\rho_{hv} \geq 0.85$ to ensure sufficient signal-to-noise ratio and good-quality data, and to regions below the environmental −20°C level to mitigate the chance of ice crystals with enhanced Z_{DR} causing false detections. Similar to the criteria used in Snyder et al. (2015) for their Z_{DR} column detection algorithm, a Z_{DR} column is defined here to exist if $Z_{DR} \geq 1.0$ dB for at least two vertically contiguous grid boxes above the environmental 0°C level. To help ensure that only legitimate Z_{DR} columns are detected and limit the chance of noise in the Z_{DR} field causing false detections, an additional 3 km × 3 km horizontal mode filter is incorporated in which only columns exhibiting $\rho_{hv} \geq 0.85$ and $1.0 \leq Z_{DR} \leq 5.0$ dB in at least five of the nine grid boxes within the filter are counted. A summary of these detection criteria is shown in Table 1.

As opposed to warming in areas with $w > -0.2$ m s^{-1} as in the existing cloud analysis, temperature adjustments are instead made anywhere Z_{DR} columns are detected. Adjustments are made both where Z_{DR} columns are located and to one grid box surrounding the Z_{DR} columns to aid in establishing wide-enough updrafts that do not mix out before becoming established. Similarly, instead of saturating based on a simple Z criterion, saturation is only applied to the model columns (within the cloud region as determined by Z) where Z_{DR} columns have been detected. Model columns surrounding detected Z_{DR} columns are also saturated, with the horizontal extent proportional to the detected depth of the columns (in this case, half the number of model levels in the detected Z_{DR} columns) to prevent the added moisture from mixing out and to attempt to add more moisture for "stronger" (i.e., taller) Z_{DR} columns. In addition to moistening and heating at observed Z_{DR} column locations, an additional drying procedure is applied in an attempt to mitigate possible overmoistening by the microphysics scheme. At any locations satisfying $Z \geq 10$ dBZ and relative humidity ≥80% but with no detected Z_{DR} column, the relative humidity is reduced by half of the excess relative humidity above 80% (e.g., if the relative humidity is 90% with no Z_{DR} column detected, the relative humidity is reduced to 85%). This is, admittedly, an arbitrary process, but remains a succinct way to provide minor drying to areas characterized by precipitation (sufficient to meet the $Z \geq$ 10-dBZ criterion) but that are outside of Z_{DR} columns (where, we hypothesize, deep updrafts are less likely). Future work will attempt to examine the sensitivity to the Z_{DR} column detection criteria and the details of the filtering and weighting procedures for moistening and drying.

TABLE 1. Summary of the criteria used to detect Z_{DR} columns.

Variable	Criteria
T	$-20° \leq T \leq 0$°C
Z	≥10 dBZ
ρ_{hv}	≥0.85
Z_{DR}	≥1.0 dB with vertical continuity

An example of the differences in potential temperature and water vapor mixing ratio analysis increments between the traditional cloud analysis and the modified cloud analysis is shown in Fig. 2 for the initial 2000 UTC assimilation cycle of the 19 May 2013 Oklahoma case (discussed below). While the magnitudes of the moistening and warming are comparable, the location and extent of the increments vary between the two. The traditional cloud analysis (Fig. 2a) shows a large area of moistening with two primary areas of warming west-northwest of Oklahoma City associated with the first developing supercell, and smaller areas of moistening and warming northwest and west-southwest of Oklahoma City. In contrast, the modified cloud analysis employing detected Z_{DR} columns (Fig. 2b) shows a smaller area of moistening and warming directly west of Oklahoma City, southwest of the area modified in the traditional cloud analysis, and with little/no moistening or warming elsewhere. The only exception is far southwest of Oklahoma City, where the modified cloud analysis shows a bit more moistening associated with developing convection than the traditional cloud analysis. While the differences in analysis increments between the traditional and modified cloud analyses vary with time, Fig. 2 provides a demonstrative example of the typical differences between the methods.

3. Experimental setup

To investigate the impact of the modified cloud analysis, two tornadic supercell events were studied: the 19 May 2013 tornado outbreak in central Oklahoma ("the OK case") and the tornadic supercell of 25 May 2016 in north-central Kansas ("the KS case").

a. Case descriptions

Around 2000 UTC 19 May 2013, thunderstorms initiated near a dryline just west of the Oklahoma City, Oklahoma, metropolitan area in an environment characterized by strong vertical wind shear and high potential convective instability (i.e., CAPE). These storms developed quickly, and the three supercells that emerged from the convection moved toward the east-northeast; two of the supercells produced a total of

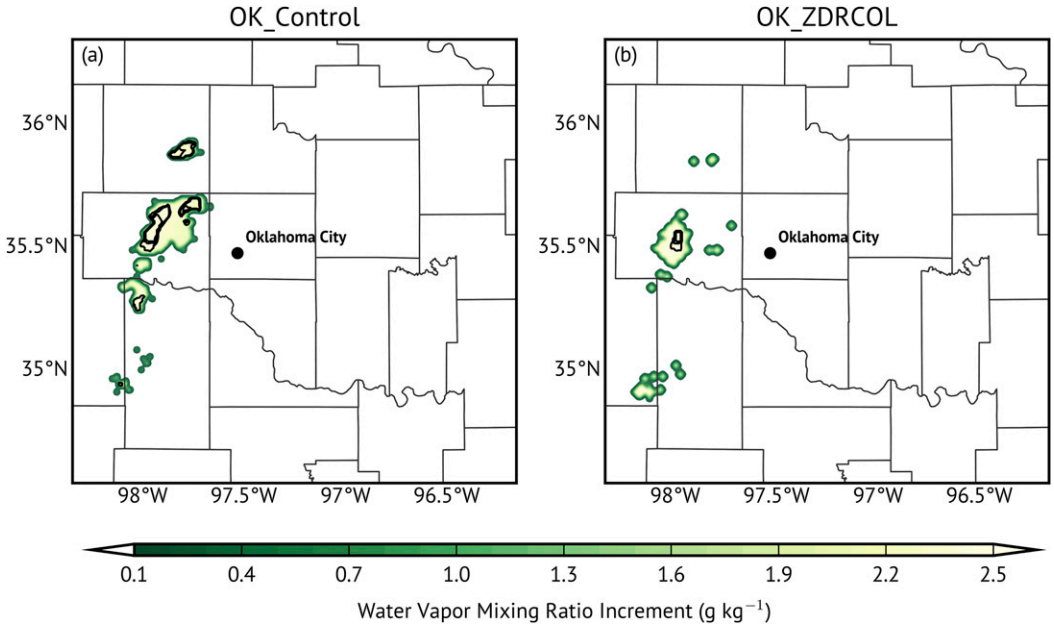

FIG. 2. The 2000 UTC analysis increments of water vapor mixing ratio (shading, g kg^{-1}) and potential temperature (black contours every 1 K) at approximately 5 km AGL for (a) the traditional cloud analysis and (b) the modified cloud analysis for the 19 May 2013 Oklahoma case.

eight tornadoes, whereas the third supercell was not tornadic. The northernmost supercell produced two brief tornadoes north and northeast of Oklahoma City before producing a long-lived tornado that produced EF3 damage near Carney, Oklahoma, between 2141 and 2224 UTC that resulted in 4 injuries; the southernmost supercell spawned a tornado that produced EF4 damage near Shawnee, Oklahoma, between 2300 and 2350 UTC that resulted in 2 fatalities and 10 injuries (NWS 2017a).

In the KS case, an isolated supercell formed in north-central Kansas just north of a warm front around 2200 UTC 25 May 2016 and moved slowly east-southeastward. The storm produced a total of four tornadoes, including a long-track tornado just east-northeast of Salina, Kansas, that lasted over 1.5 h (0007–0140 UTC) (NWS 2017b).

For both cases, observed tornado tracks are retrieved from shapefiles created from damage survey reports.

b. *Model setup*

The model used in this study is the ARPS (Xue et al. 2000, 2001, 2003), a nonhydrostatic, compressible, numerical model designed to function at multiple scales with an emphasis on the explicit prediction of convection. Terrain data were derived from the U.S. Geological Survey 3-arc-s dataset. Subgrid-scale turbulence was parameterized using a 1.5-order TKE turbulence scheme, with the evolution of the planetary boundary layer using the formulation of Sun and Chang (1986). Cloud microphysics were parameterized using the Milbrandt–Yau double-moment scheme (Milbrandt and Yau 2005a,b), and both short- and longwave radiation were parameterized using the NASA Goddard schemes (Chou 1990, 1992). A two-layer force-restore soil model based on Noilhan and Planton (1989) was used with surface fluxes based on stability-dependent drag coefficients using surface temperature and volumetric water content. More information about the full ARPS physics suite can be found in Xue et al. (2001).

Experiments were conducted using a one-way nested grid configuration. The parent domain has a size of 1200 km × 1200 km with a horizontal grid spacing of 4 km, and the inner nest a size of 500 km × 500 km with a horizontal grid spacing of 1 km. The domains for the OK and KS cases were centered on 35.45°N, 97.25°W and 38.65°N, 97.55°W, respectively. Both nests used a stretched vertical grid containing 53 vertical levels with an average spacing of 400 m and a minimum spacing of 100 m near the surface. The model top was rigid with a Rayleigh damping layer above 12 km to absorb vertically propagating waves. Lateral boundary conditions were externally forced. The simulated Z fields were computed using the T-matrix-based algorithm of Jung et al. (2010a). The domains used for each case are shown in Fig. 3, and a summary of the model setup used for these experiments is provided in Table 2.

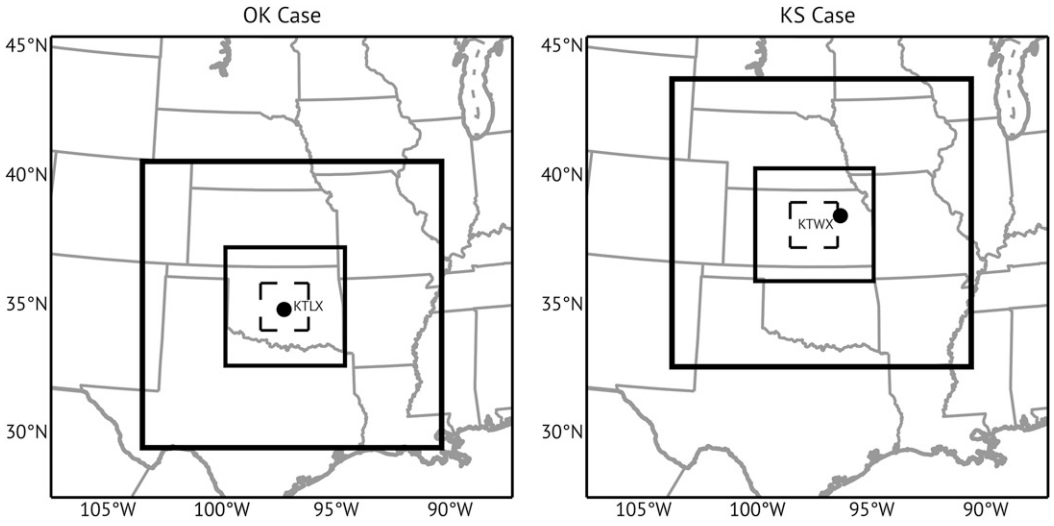

FIG. 3. Model domains used for the (left) 19 May 2013 Oklahoma case and the (right) 25 May 2016 Kansas case. The larger outer nest is shown in a thick black line, the inner nest is shown in a thin black line, and the zoomed-in domain plotted in subsequent figures is shown with a dotted line. The radar site used for each case is labeled.

c. *Assimilation procedures*

The 12-km North American Mesoscale Forecast System (NAM) model analysis and forecast data were used to initialize the parent domain. For the OK case, the 1800 UTC 19 May 2013 NAM analysis was used, and for the KS case the 2-h forecast from the 1800 UTC 25 May 2016 NAM analysis (valid at 2000 UTC) was used. The NAM data were interpolated onto the 4-km ARPS grid, which was then integrated forward for 1 h using 3-h lateral boundary conditions derived from the NAM. This forecast was then further interpolated down to the inner nest and integrated forward another 1 h, with boundary conditions on the inner nest updated at 30-min intervals from the outer nest, for a total spinup period of 2 h. This forecast was then used as the background for all assimilation experiments performed.

Assimilation cycles were performed every 10 min following Hu and Xue (2007), who found this to be the optimal cycling frequency in their experiments. Radial velocity data were assimilated using the ARPS 3DVAR routine (Gao et al. 2004; Hu et al. 2006b), after which the cloud analysis routine was called. For the OK case, Oklahoma Mesonet data (Brock et al. 1995) were also assimilated using the 3DVAR routine. After 30 min, a separate 1-h forecast was made, with 10-min assimilation cycles continuing. Then 1-h forecasts were subsequently initiated every 30-min for 3 h after the initial analysis time. A diagram of the spinup, cycling, and assimilation process is shown in Fig. 4. For the OK case, radar data from the Twin Lakes, Oklahoma, WSR-88D (KTLX) were used, while the KS case used data from the Topeka, Kansas, WSR-88D (KTWX) (Fig. 3). For each case, two runs were performed: a control run (hereafter "Control"), in which the legacy cloud analysis is used (see section 2b), and an experimental run (hereafter "ZDRCOL"), which employed the modified polarimetric cloud analysis described in section 2c.

Specific nomenclature for each experiment will be referred to hereafter by their case and which cloud analysis method was used (i.e., "KS_ZDRCOL" refers to the 25 May 2016 KS case experiment employing the modified cloud analysis).

4. Results

a. *19 May 2013 case*

To investigate the performance of the Z_{DR} column detection algorithm, a composite plot of remapped 1-km Z and analyzed Z_{DR} column depth from the KTLX radar observations in 10-min intervals for the assimilation period is shown in Fig. 5. Each of the three swaths associated with a supercell is labeled and will be used to reference each storm in the subsequent discussions. The 15-dBZ contour is shown as that is the default threshold for saturation in the original cloud analysis routine. Distinct Z_{DR} column tracks are evident for all three main storms, with all storms exhibiting prominent Z_{DR} columns during their formative stages before becoming more intermittent, supporting the use of Z_{DR} columns for spinning up storms in the model early in their life cycle. In each case, the Z_{DR} column is found on the southwest flank of the storm where the main updraft is expected to be located.

TABLE 2. Summary of ARPS model setup used for all experiments.

Model parameter	Value/description	
	Control	ZDRCOL
Outer horizontal domain size	1200 × 1200	
Outer horizontal grid spacing	$\Delta x = \Delta y =$ 4 km	
Inner horizontal domain size	500 × 500	
Inner horizontal grid spacing	$\Delta x = \Delta y =$ 1 km	
Vertical grid spacing	Stretched grid with mean $\Delta z =$ 400 m and minimum $\Delta z =$ 100 m across 53 levels	
Time step	2 s	
Physics	Nonhydrostatic	
Coriolis	On	
Computational mixing	Fourth order	
Lateral boundary conditions	Externally forced	
Upper boundary condition	Rigid top with Rayleigh damping layer at $z =$ 12 000 m	
Microphysics	Milbrandt–Yau double-moment scheme (Milbrandt and Yau 2005a,b)	
Radiation	NASA Goddard shortwave and longwave schemes (Chou 1990, 1992)	
Surface	Surface fluxes dependent on stability, temperature, and volumetric water content	
Turbulence	1.5-TKE scheme with Sun and Chang (1986) boundary layer scheme	
Cloud analysis	Legacy	Modified (see Table 1)

The only exception to this is for the weakening and fast-moving cell north of Oklahoma City that propagates to the left of the mean wind off to the north-northeast. The supercell that begins to the west of Oklahoma City ("Supercell 1" in Fig. 5) exhibits a large, deep Z_{DR} column from its inception that travels toward the northeast and then turns to the east-northeast before producing the first tornado. The Z_{DR} column then shrinks and becomes shallower near and after the first tornado dissipates; the Z_{DR} column associated with the main updraft becomes more robust shortly after the genesis of the second tornado east-northeast of Oklahoma City, near the observed track. Two more Z_{DR} column tracks are apparent south of Oklahoma City, with the middle track ("Supercell 2") associated with a smaller Z_{DR} column as it tracked northeast. The southernmost storm ("Supercell 3") exhibited a larger and taller Z_{DR} column that suddenly weakened and never fully reappeared. The period analyzed here ends at 2300 UTC, the approximate start time of the long-track southern tornado southeast of Oklahoma City. However, no clear Z_{DR} column is evident here due to the close proximity of the updraft to the radar (i.e., the Z_{DR} column likely was located within the cone of silence, which extends 12 km from the radar at a height of 4 km AGL), although additional obfuscation by hail or tornadic debris cannot be ruled out. This is a known drawback that should be taken into consideration when using any methods that use vertically integrated data or echo-top heights from a single radar.

The areas encompassed by the 15-dBZ threshold are much larger and extend farther to the north and east of the analyzed Z_{DR} columns. Note that for this and all subsequent figures for the OK case the two easternmost tornadoes (shown in gray in Fig. 5) occurred after the period examined in this experiment.

Composite plots of the maximum analyzed w (contoured at 30 m s^{-1}) at each grid point for both OK_Control and OK_ZDRCOL through the assimilation period (2000–2300 UTC) are shown in Fig. 6. OK_Control exhibits a rather noisy w field composed of many spurious updrafts, along with a pronounced northward bias compared to the observed tornado tracks. This northern and positive forward speed bias has been observed in many storm-scale modeling studies (e.g., Potvin et al. 2014; Xue et al. 2014; Stratman and Brewster 2015; Wheatley et al. 2015). In sharp contrast, OK_ZDRCOL features much more consolidated updraft tracks that closely follow the analyzed Z_{DR} column paths (and observed tornado tracks). As in Fig. 5, the final analysis included is at 2300 UTC near the beginning of the long-track tornado southeast of Oklahoma City, evident with a large and strong updraft in excess of 40 m s^{-1} near the start of the tornado track that is not as apparent in OK_Control. The 30 m s^{-1} contours also appear to be larger in OK_ZDRCOL than in OK_Control, suggesting wider, stronger updrafts.

The composited 1–6 km above ground level (AGL) updraft helicity (Kain et al. 2008) swaths for three different forecast periods are shown in Fig. 7. Model output was saved every 5 min and composited over the 1-h forecast, with the maximum for the forecast period shown at each grid point. The 1–6-km updraft helicity provides a reasonable depiction of the path of mesocyclones and overall storm track. To aid in verifying the forecast updraft helicity swaths, rotation tracks derived from the Multi-Radar Multi-Sensor (MRMS; Smith et al. 2016) system, which are composited maximum values of radar-derived azimuthal shear (Smith and Elmore 2004) in a layer through a given time period, are included in Fig. 7. While the traditional azimuthal shear product uses 0–2- or 3–6-km AGL layers, the 1–6-km AGL azimuthal shear was used in this study to better correspond with the 1–6-km updraft helicity derived from the model output. The rotation tracks shown in Fig. 7 correspond to the 1-h forecast periods shown in each panel.

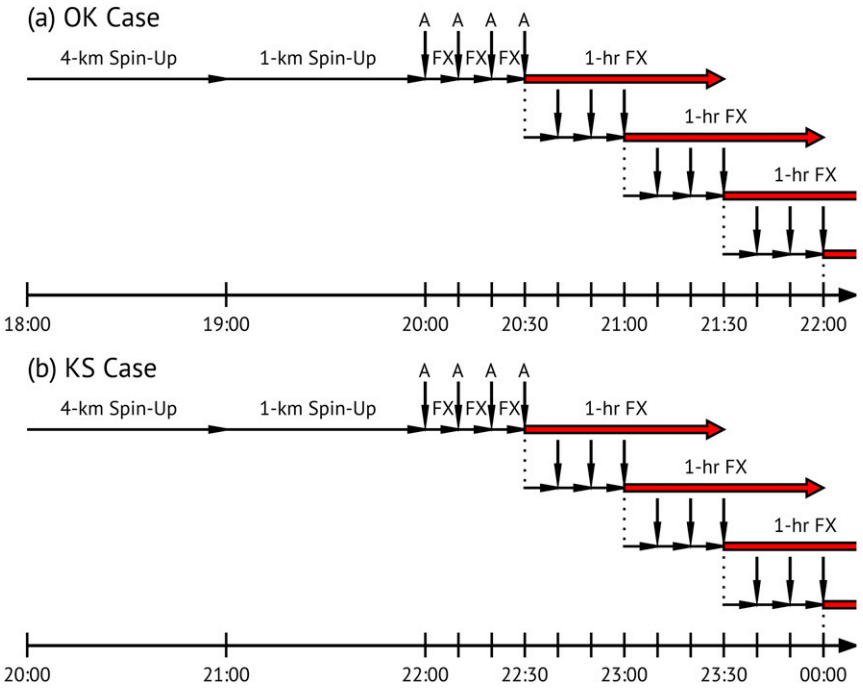

FIG. 4. Diagram showing the spinup and assimilation cycles used for the (a) OK case and the (b) KS case. "FX" represents forecasts, while "A" represents assimilation cycles encompassing the ARPS 3DVAR + Cloud Analysis routines. The 0–1-h forecasts initiated every 30 min are denoted by red arrows. The dotted lines indicate a continuation of the 10-min assimilation cycles in addition to the initiated 0–1-h forecast.

During the first 0–1-h forecast at 2030 UTC (Figs. 7a,b), both OK_Control and OK_ZDRCOL feature a storm track for Supercell 1 that is located too far north. The updraft helicity swath in OK_ZDRCOL, however, is more consolidated and features a smaller northward bias compared to OK_Control. Supercell 1 in OK_ZDRCOL has a slower mean storm motion, with the center of the updraft helicity swath covering approximately 10 fewer kilometers than OK_Control during the forecast period. Finally, OK_ZDRCOL features a weak updraft helicity swath associated with the second developing storm (Supercell 2, southwest of Oklahoma City) that is absent in the OK_Control run.

The improvements of OK_ZDRCOL over OK_Control are most pronounced in the forecast initiated at 2130 UTC (Figs. 7c,d), approximately 10 min before the start of the long-track tornado northeast of Oklahoma City. OK_Control features multiple updraft helicity swaths. There is no identifiable strong updraft helicity swath coincident with the observed rotation track of Supercell 1, with instead a very strong and prominent updraft helicty swath displaced far to the northeast of the observed rotation track and corresponding tornado. Moreover, there are two notable updraft helicity swaths corresponding to the weakening rotation track of Supercell 2 southeast of Oklahoma City, with no updraft helicity swath that clearly corresponds with the rotation track for Supercell 3. In stark contrast, OK_ZDRCOL captures the updraft helicty swath of Supercell 1 well, with the forecast swath nearly coincident with the observed rotation track and with only a slight bias in forward speed. It also correctly captures the updraft helicity swath associated with Supercell 2 that weakens as it moves to the northeast. Finally, the early development of strong rotation in the southernmost supercell (Supercell 3) that would go on to produce the Shawnee tornado is depicted to the south of Oklahoma City while being absent in OK_Control.

The 2230 UTC 0–1-h forecast (Figs. 7e,f) show many of the same improvements. Both Supercells 1 and 2 were nontornadic and beginning to weaken, with less pronounced updraft helicity swaths in OK_ZDRCOL. In contrast, OK_Control has strong but noisy updraft helicity swaths for these storms displaced to the northeast of their observed locations. For Supercell 3, both OK_Control and OK_ZDRCOL exhibit updraft helicity associated with the strong and broad observed rotation track south of Oklahoma City. However, the updraft helicity swath in OK_Control is primarily north and east of the observed rotation track, while

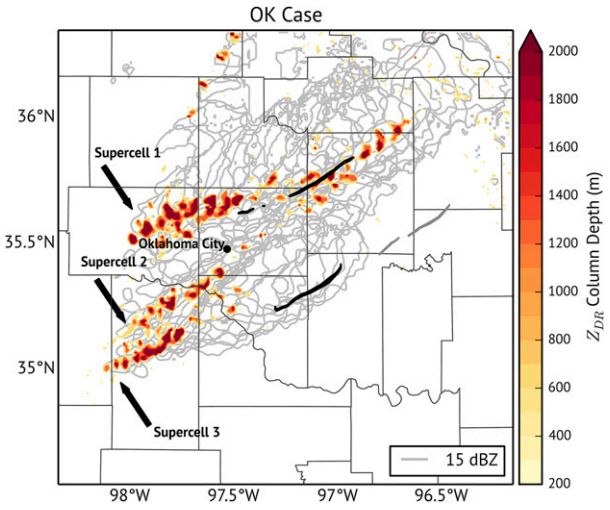

FIG. 5. Composited remapped Z (15-dBZ contour in gray) and analyzed Z_{DR} column depth (color shaded, in m, and defined as the height of the 1.0-dB surface above the environmental 0°C level) between 2000 and 2300 UTC in 10-min intervals for the 19 May 2013 case using the detection criteria listed in Table 1. Observed tornado tracks are shown in black and gray, with gray tracks indicating observed tornadoes that fall outside of the period of study.

OK_ZDRCOL captures the rotation (albeit with a slight north bias) and its timing well.

To further examine the improvements in the OK_ZDRCOL forecasts over OK_Control, the 1-km AGL Z is shown for the forecasts initiated at 2130 UTC in 20-min increments and compared to the observed radar fields in Fig. 8. This time period represents the duration of the northern long-track tornado northeast of Oklahoma City, which was on the ground between 2141 and 2224 UTC, as well as the leadup period to the long-track tornado produced by Supercell 3, which first touched down at 2300 UTC. For both the OK_Control and OK_ZDRCOL runs, an adjustment period is seen in the first 20 min (Figs. 8e,f) with small, yet intense, precipitation cores ($Z \geq 65$ dBZ) present. These high values of Z occur within the core of the middle and northern storms (Supercells 1 and 2) in OK_Control (Fig. 8e), while in OK_ZDRCOL these high Z values are predominantly near the southern flank of the storms and/or within the hook echoes, where the Z_{DR} columns were analyzed. Later in the forecast period (2210–2230 UTC), it is again clear that the OK_Control run features a northward and positive forward speed bias (Figs. 8h,k) compared to the observations (Figs. 8g,j). Supercell 2 fails to remain distinct, and by 2230 UTC unobserved banding features are seen in the OK_Control run (Fig. 8k). The storms are also larger than those observed, with large areal coverage of $Z \geq 45$ dBZ. In contrast, the OK_ZDRCOL run is much closer to the observations. While a small northeastward bias does still exist, the forecast storms are in better agreement with the observations in terms of size and position, with three distinct storms featuring

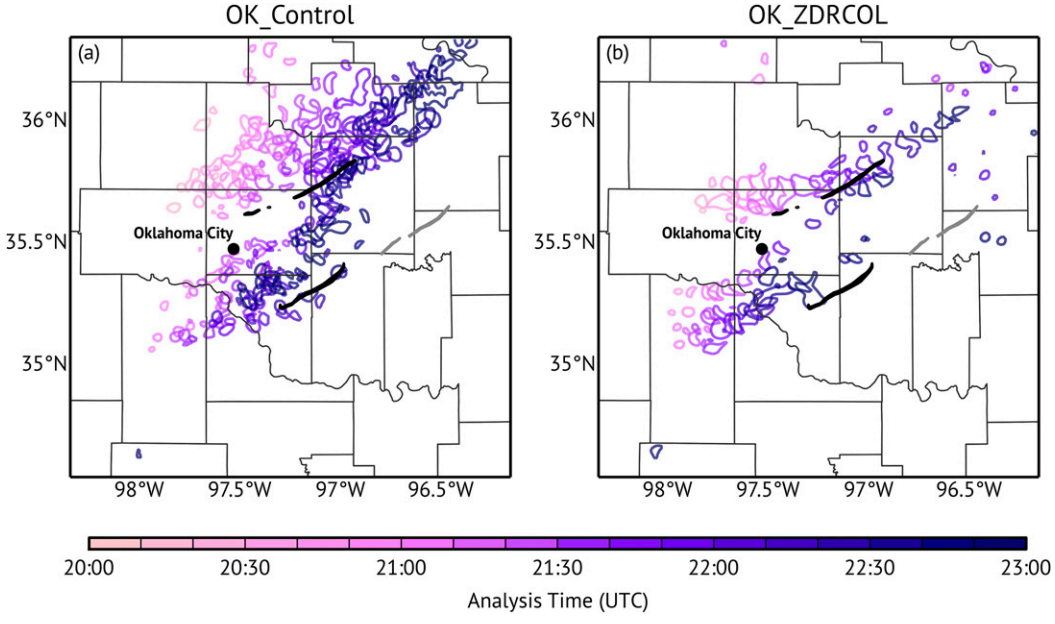

FIG. 6. Composited maximum vertical velocity in each grid column for each of the postassimilation analyses from 2000 to 2300 UTC for the 19 May 2013 case for the (a) OK_Control case and (b) OK_ZDRCOL case, colored according to their corresponding analysis time and showing the 30 m s^{-1} vertical velocity contour line. Observed tornado tracks are shown in black and gray, with gray tracks indicating observed tornadoes that fall outside of the period of study.

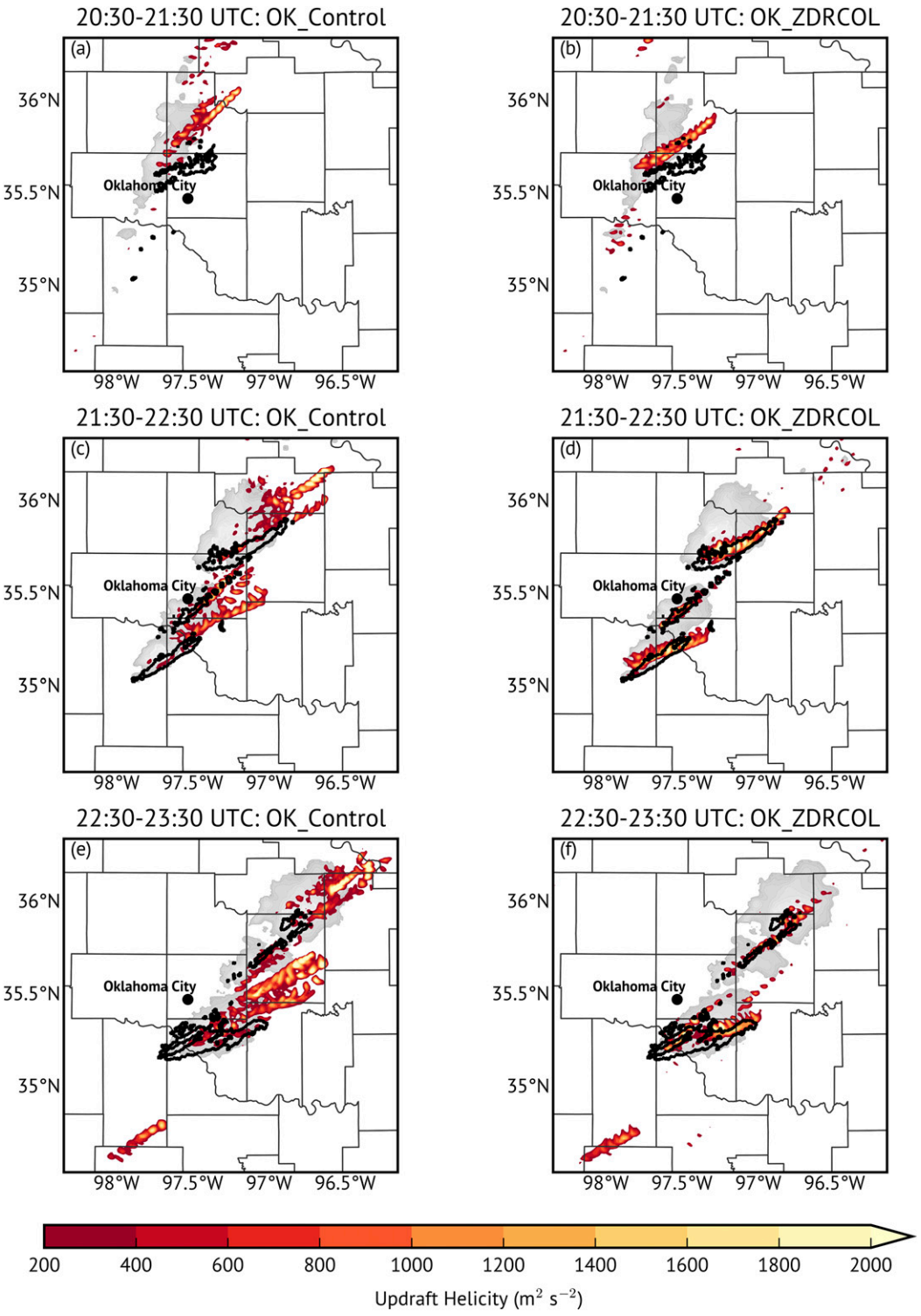

FIG. 7. Composited 1–6-km AGL updraft helicity ($m^2 s^{-2}$, red shading) at each grid point for (a),(c),(e) OK_Control and (b),(d),(f) OK_ZDRCOL for the 0–1-h forecasts beginning at (a),(b) 2030; (c),(d) 2130; and (e),(f) 2230 UTC. MRMS-derived 1–6-km AGL rotation tracks (black contours, 0.01 s^{-1} shown) are included for each 1-h period. The initial 1-km Z of each 1-h period is shown for reference (grayscale shading).

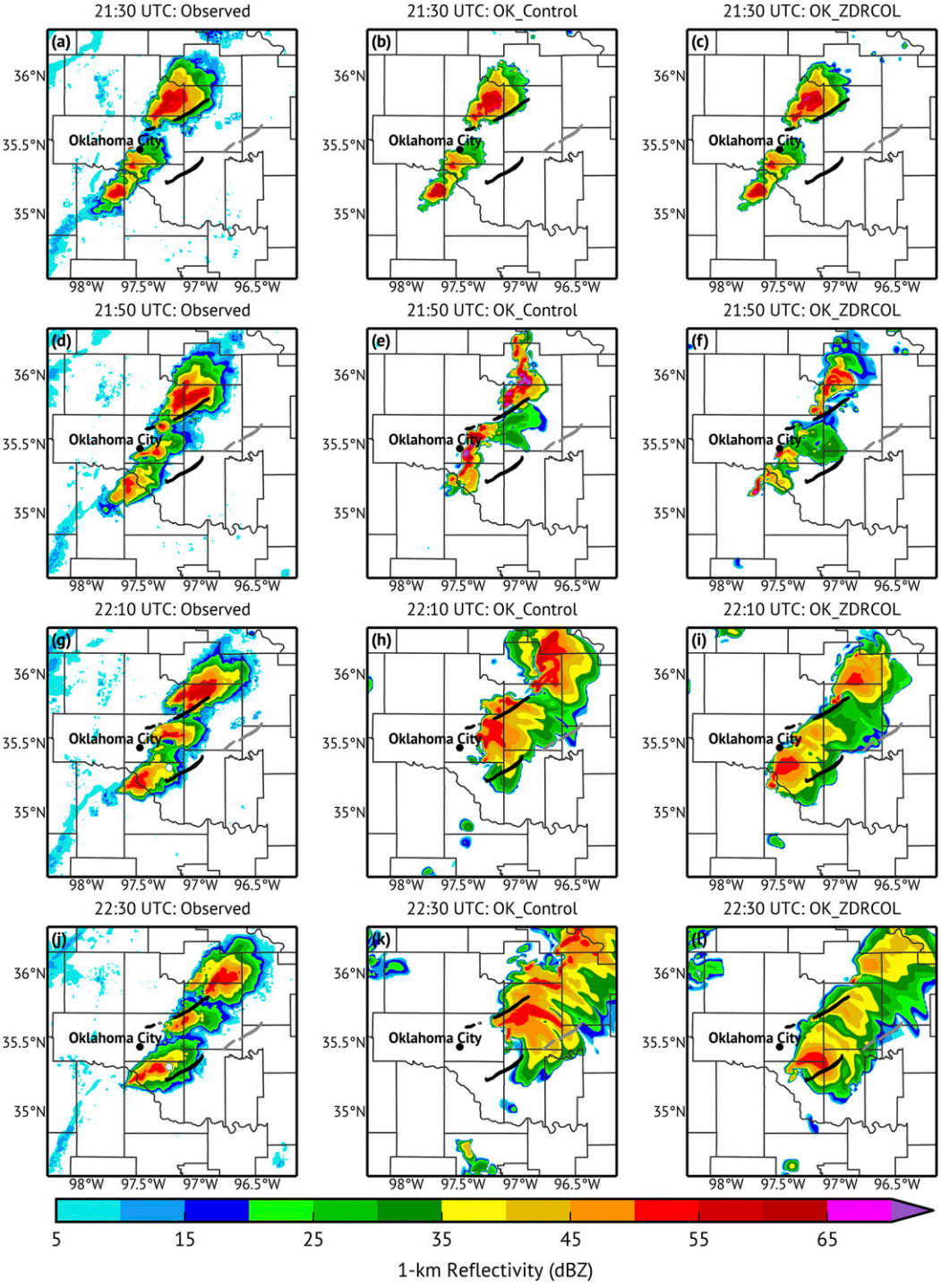

FIG. 8. Plots of (left) observed 1-km AGL Z from KTLX remapped to the ARPS grid, and corresponding forecasts from the (middle) OK_Control and (right) OK_ZDRCOL runs for the 0–1-h forecast beginning at 2130 UTC for the 19 May 2013 case. Plots are shown for (a)–(c) the analysis at 2130 UTC, (d)–(f) 20-min forecast at 2150 UTC, (g)–(i) 40-min forecast at 2210 UTC, and (j)–(l) 60-min forecast at 2230 UTC. Observed tornado tracks are shown in black.

identifiable hook echoes and broad supercellular features present 1 h into the forecast (Fig. 8l).

Based on these encouraging qualitative results, the equitable threat scores (ETS) and frequency biases were computed for a quantitative look at the performance of OK_Control and OK_ZDRCOL. The ETS, also known as the Gilbert skill score (Gilbert 1884), is given by

$$\mathrm{ETS} = \frac{H - H_{\mathrm{rdn}}}{M + F + H - H_{\mathrm{rdn}}}, \tag{1}$$

where H is the number of hits, M is the number of misses, F is the number of false alarms, and H_{rdn} is the number of hits expected due to random chance, given by

$$H_{\mathrm{rdn}} = \frac{(H + M)(H + F)}{N}, \tag{2}$$

where N is the total number of forecast points included in the calculation. The ETS is calculated on a gridpoint basis satisfying or exceeding a defined (here Z) threshold, with a value of 1.0 indicating a perfect forecast and 0.0 indicating no forecast skill. The bias is calculated from

$$\mathrm{Bias} = \frac{H + F}{H + M} - 1 \tag{3}$$

and provides a ratio of the number of forecast grids and the number of observed grids exceeding a threshold, normalized to zero. A bias of zero indicates no bias, while a positive bias indicates an overestimate of Z exceeding a threshold. Both the ETS and bias were calculated for the composite Z at 20-, 30-, and 40-dBZ thresholds and are shown for the OK case in Fig. 9. Note that the ETS at the analysis time is not necessarily equal to 1.0 due to both smoothing procedures and differences in how Z is calculated: the observations are being compared against simulated Z derived from a T-matrix code for the single-species hydrometeor distribution that was retrieved from the cloud analysis. The ETS for the 20-dBZ threshold (Fig. 9a) are comparable between the two experiments, but notable improvements in ETS are seen in OK_ZDRCOL over OK_Control for high Z thresholds (Figs. 9c,e). The ETS for OK_ZDRCOL remains superior for the entire 1-h duration of every forecast, showing a noteworthy positive impact of Z_{DR} column assimilation. Both OK_Control and OK_ZDRCOL exhibit generally positive biases that increase with time at all three Z thresholds. For all forecasts at all times, however, OK_ZDRCOL features lower biases (Figs. 9b,d,f). This tendency toward lower Z biases in OK_ZDRCOL is also seen in 1-km Z for the 2130 UTC forecast (Fig. 8).

b. 25 May 2016 case

The KS case presents a somewhat more challenging forecast scenario owing to a complex evolution of the supercell and the greater distance between the supercell and the radar. After becoming mature, the main supercell began moving slowly to the southeast. A new storm developed to the southwest of the main supercell, which produced a left-moving supercell that moved off to the north-northeast before merging with the primary supercell. Additional convection also formed along, and was absorbed into, the southern flank of the forward-flank downdraft in the supercell. This storm was farther away from the radar than the storms in the OK case were (initiation occurred approximately 140 km away from the radar compared to 65 km away from the radar in the OK case), resulting in a decrease of the quality of radar data available for assimilation due to both decreased low-level coverage and increasing radar resolution volume ($\approx$0.22 km^3 at a 65-km range vs $\approx$1.01 km^3 at a 140-km range for a 0.5° elevation angle). Additionally, in contrast to the OK case, this case lacked the assimilation of mesonet surface observations.

A long, continuous swath of Z_{DR} columns are shown for the duration of the period analyzed in the southwest corner of the supercell where the main updraft is expected to be located (Fig. 10). The Z_{DR} column's width and depth increases shortly before the start of the long-track tornado northeast of Salina, and the Z_{DR} column remains broad and deep until the end of the tornado, near the end of the assimilation period. A second Z_{DR} column swath is seen with the left split of the supercell as it moves off to the north-northeast. This column weakens near the end of the assimilation period, and the storm weakened shortly thereafter. As in the OK case, the easternmost tornado falls outside the analyzed period for this case.

The composite plot of maximum w in the analyses for the KS case shows many of the same improvements documented in the OK case. The KS_Control case shows a more disorganized and less coherent updraft path, with many spurious updrafts to the north of the main supercell path and observed tornado tracks (Fig. 11a). Considering that the end of the assimilation period is near the ending time of the long-track tornado, the general progression of the analyzed updrafts is also too fast. In contrast, KS_ZDRCOL features a much more coherent updraft swath with a slower forward motion to the east-southeast and a path closer to the observed tornado track (Fig. 11b). KS_ZDRCOL also features less spurious convection than KS_Control in the central and southern parts of the domain.

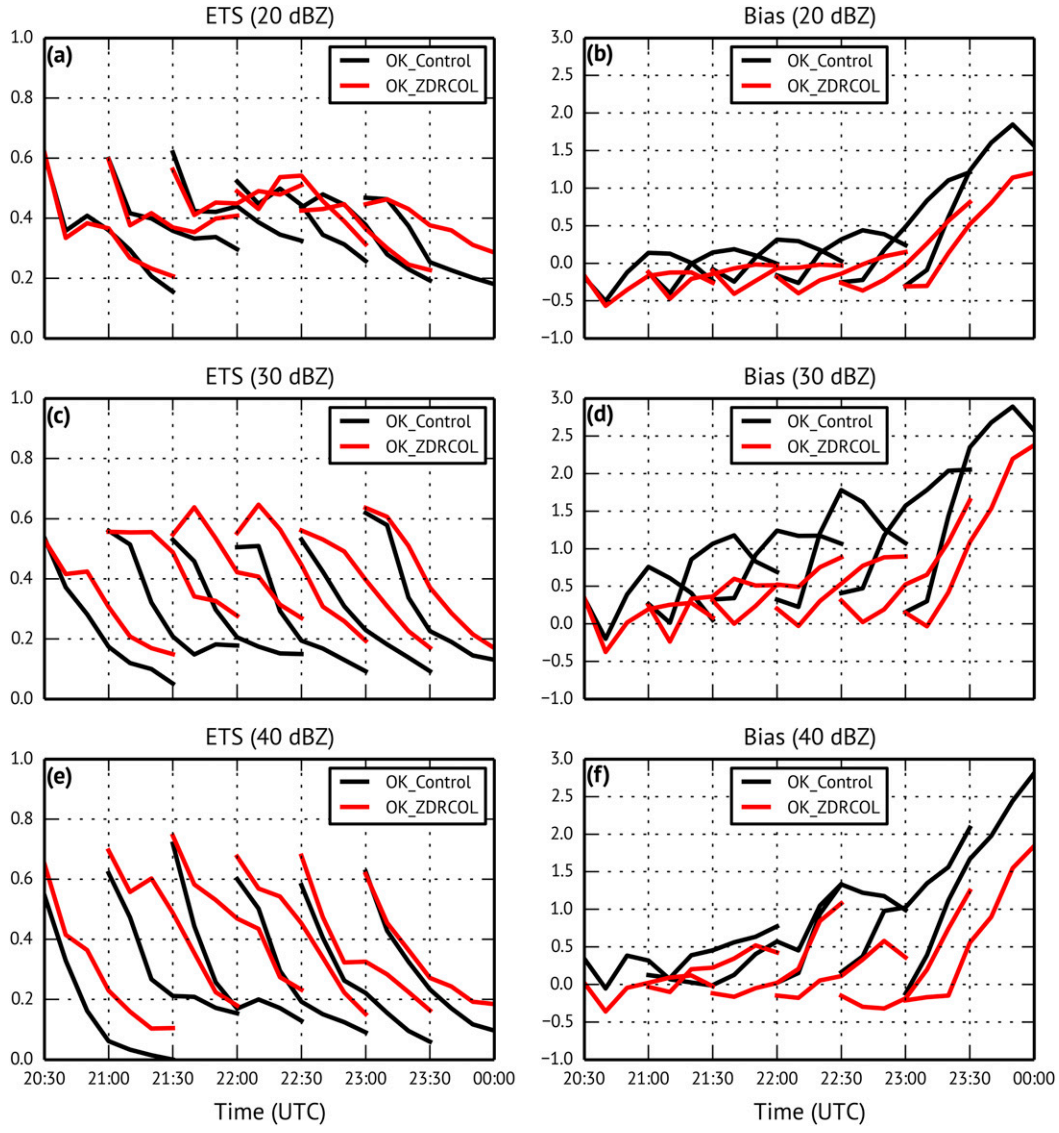

FIG. 9. Equitable threat score and bias of composite Z at (a),(b) 20-; (c),(d) 30-; and (e),(f) 40-dBZ thresholds for each of the 0–1-h forecasts for the OK case.

A comparison of 1–6-km updraft helicity with MRMS-derived rotation tracks, similar to Fig. 7, is shown for the KS case in Fig. 12. The forecasts selected here were chosen to coincide with the long-track tornado. In the forecast initiated at 2300 UTC (Figs. 12a,b), both KS_Control and KS_ZDRCOL produce a developing supercell north of Salina with an unorganized updraft and an east-northeast motion. The observed rotation tracks show only slight, messy rotation during this period. Starker differences are apparent for the 0000 UTC forecast (Figs. 12c,d). KS_Control features a disorganized updraft helicity swath displaced far to the north of the observed rotation track. In contrast, KS_ZDRCOL features a consolidated updraft helicity swath through the duration of the forecast period along and just north of the observed rotation track, although a slight slow bias in forward speed is apparent. These same general patterns are also observed for the 0100 UTC forecast, with a noisy updraft helicity field too far to the northeast in KS_Control; KS_ZDRCOL exhibits a large, southeastward-directed updraft helicity swath displaced slightly southwest of the observed rotation track.

An example of observed and forecast Z for both KS_Control and KS_ZDRCOL is shown in Fig. 13 for the 0000 UTC forecast. This 1-h period begins near the start time of the primary long-track tornado and features a complex evolution involving the secondary storm to the

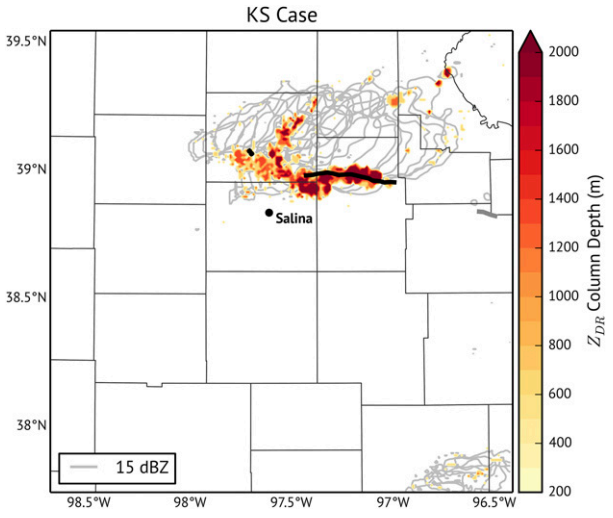

FIG. 10. Composited remapped Z (15-dBZ contour in gray) and analyzed Z_{DR} column depth (color shaded, in m) between 2200 and 0100 UTC in 10-min intervals for the 25 May 2016 case using the detection criteria listed in Table 1. Observed tornado tracks are shown in black and gray, with gray tracks indicating observed tornadoes that fall outside of the period of study.

southwest splitting and merging with the main supercell (Figs. 13a,d,g,j). As such, both KS_Control and KS_ZDRCOL struggle to accurately predict the evolution of the storm during this period. A very large and elongated forward-flank downdraft not seen in the radar observations quickly develops and extends to the east-southeast and east-northeast in KS_Control and KS_ZDRCOL, respectively. This forward-flank precipitation appears to stem from weak upper-level Z in the anvil in the observations. Despite this, KS_ZDRCOL features a more realistic supercell structure 20-min into the forecast (Fig. 13f) compared to KS_Control (Fig. 13e), with a well-defined hook echo and rear-flank downdraft near the observed tornado track. Neither KS_Control nor KS_ZDRCOL clearly capture the left-splitting supercell. An erroneous region of moderate Z (i.e., 25–35 dBZ) within the inflow region of the supercell is also seen in the KS_Control run (Fig. 13e) that is not seen in the KS_ZDRCOL run. Both KS_Control and KS_ZDRCOL generally feature Z values that are too low (by 5–10 dBZ) compared to observations outside of the forward-flank downdraft. Overall, KS_ZDRCOL features a slower and noticeably more accurate forecast track of the hook echo than KS_Control (as also seen Figs. 12c,d), as well as a more realistic looking hook echo (Figs. 13i,l vs Figs. 13h,k).

Quantitatively, KS_ZDRCOL generally exhibits improvements over KS_Control with higher ETS scores and lower biases, although the improvements in ETS scores are more mixed than in the OK case, with lower scores for the first two forecasts in the period (Fig. 14).

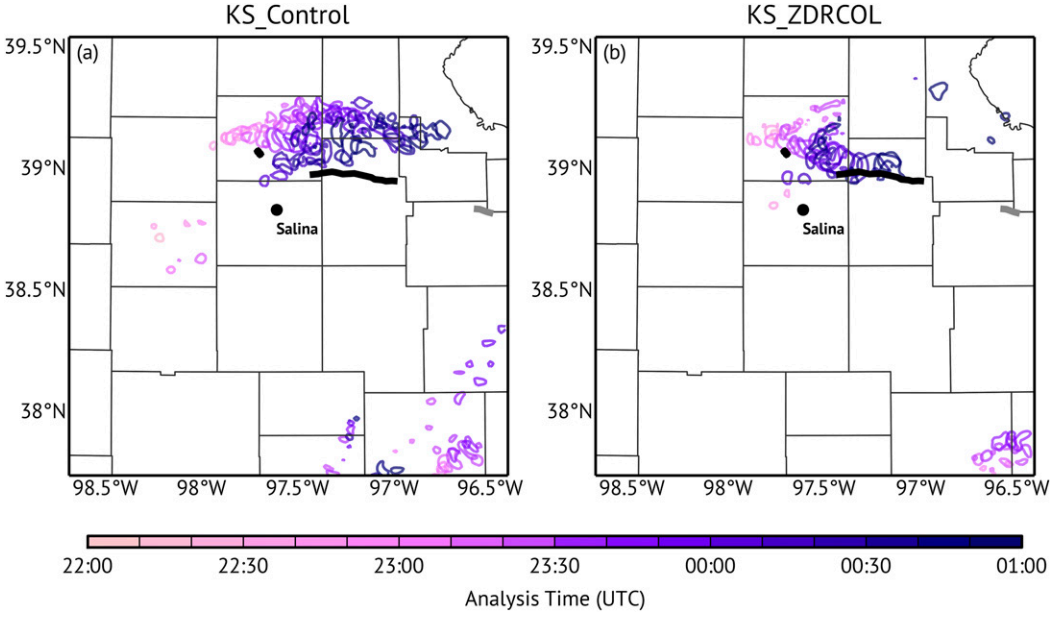

FIG. 11. Composited maximum vertical velocity in each grid column for each of the postassimilation analyses from 2200 to 0100 UTC for the 25 May 2016 case for the (a) KS_Control case and (b) KS_ZDRCOL case, colored according to their corresponding analysis time and showing the 30 m s^{-1} vertical velocity contour line. Observed tornado tracks are shown in black and gray, with gray tracks indicating observed tornadoes that fall outside of the period of study.

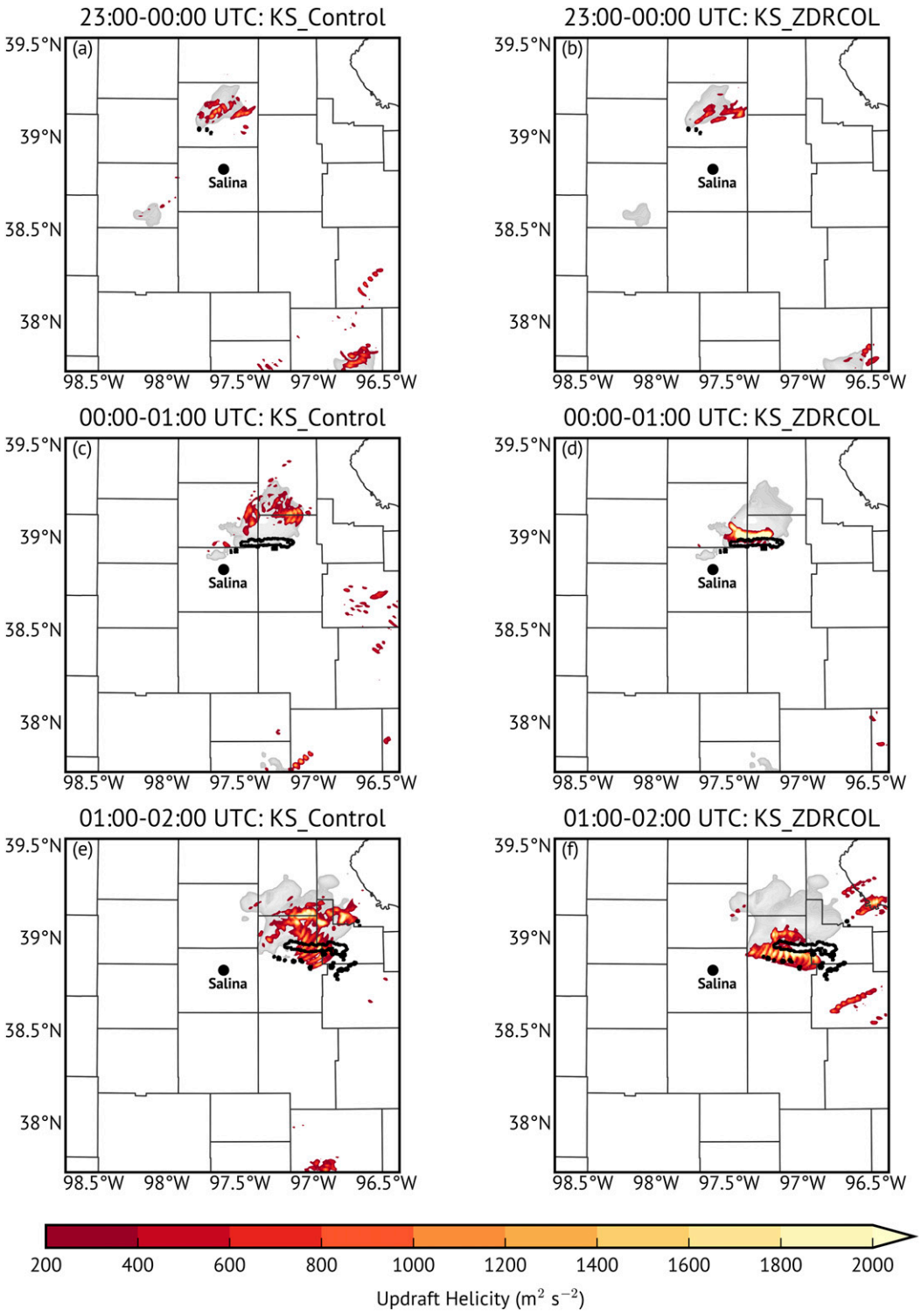

FIG. 12. Composited 1–6-km AGL updraft helicity ($m^2 s^{-2}$, red shading) at each grid point for (a),(c),(e) KS_Control and (b),(d),(f) KS_ZDRCOL for the 0–1-h forecasts beginning at (a),(b) 2300; (c),(d) 0000; and (e),(f) 0100 UTC. MRMS-derived 1–6-km AGL rotation tracks (black contours, $0.01 s^{-1}$ shown) are included for each 1-h period. The initial 1-km Z of each 1-h period is shown for reference (grayscale shading).

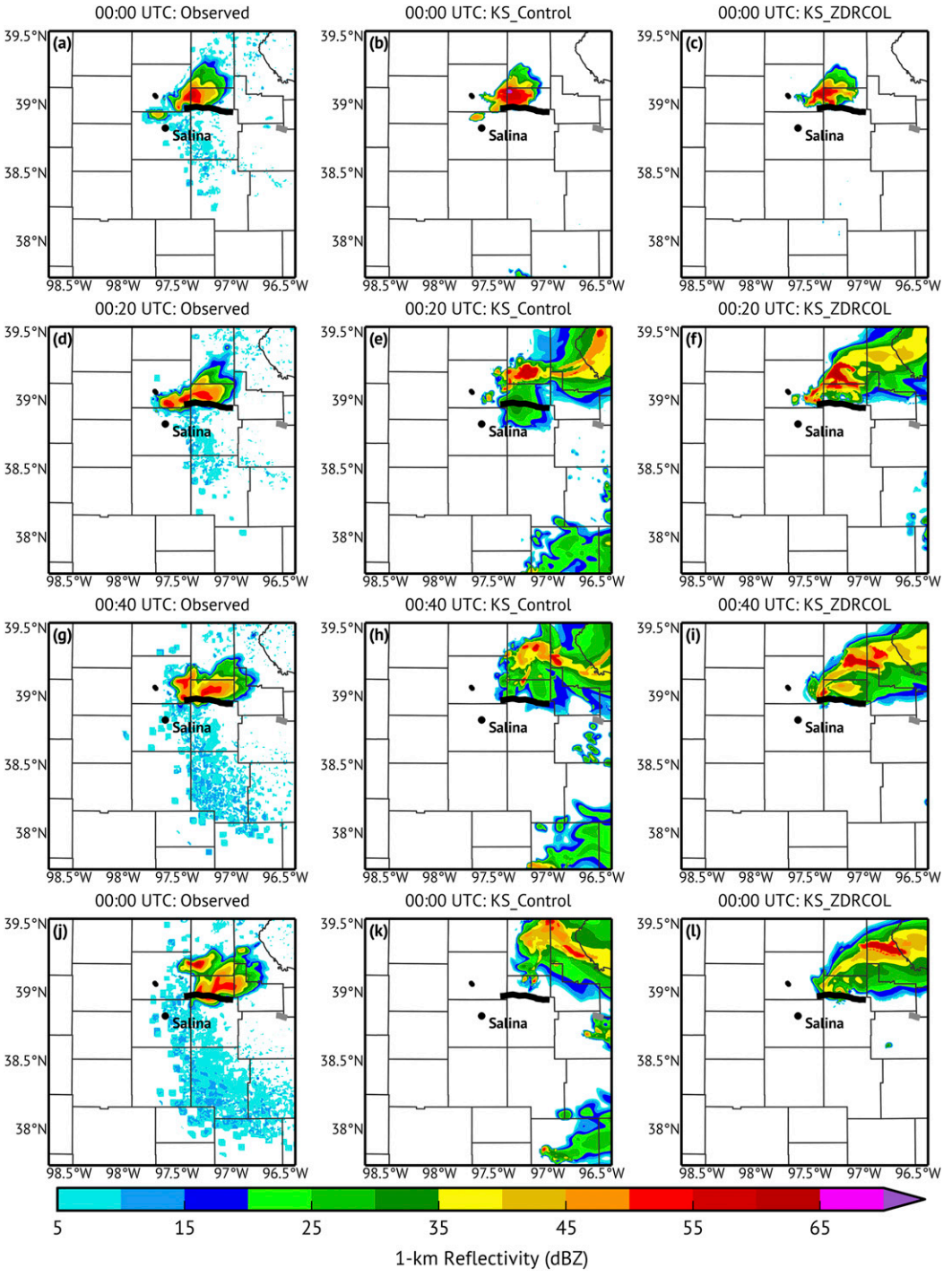

FIG. 13. (left) Observed 1-km AGL Z from KTWX remapped to the ARPS grid, and corresponding forecasts from the (middle) KS_Control and (right) KS_ZDRCOL runs for the 0–1-h forecast beginning at 0000 UTC (on 26 May) for the 25 May 2016 case. (a)–(c) The analysis at 0000 UTC, (d)–(f) 20-min forecast at 0020 UTC, (g)–(i) 40-min forecast at 0040 UTC, and (j)–(l) 60-min forecast at 0100 UTC. Observed tornado tracks are shown in black and gray, with gray tracks indicating observed tornadoes that fall outside of the period of study.

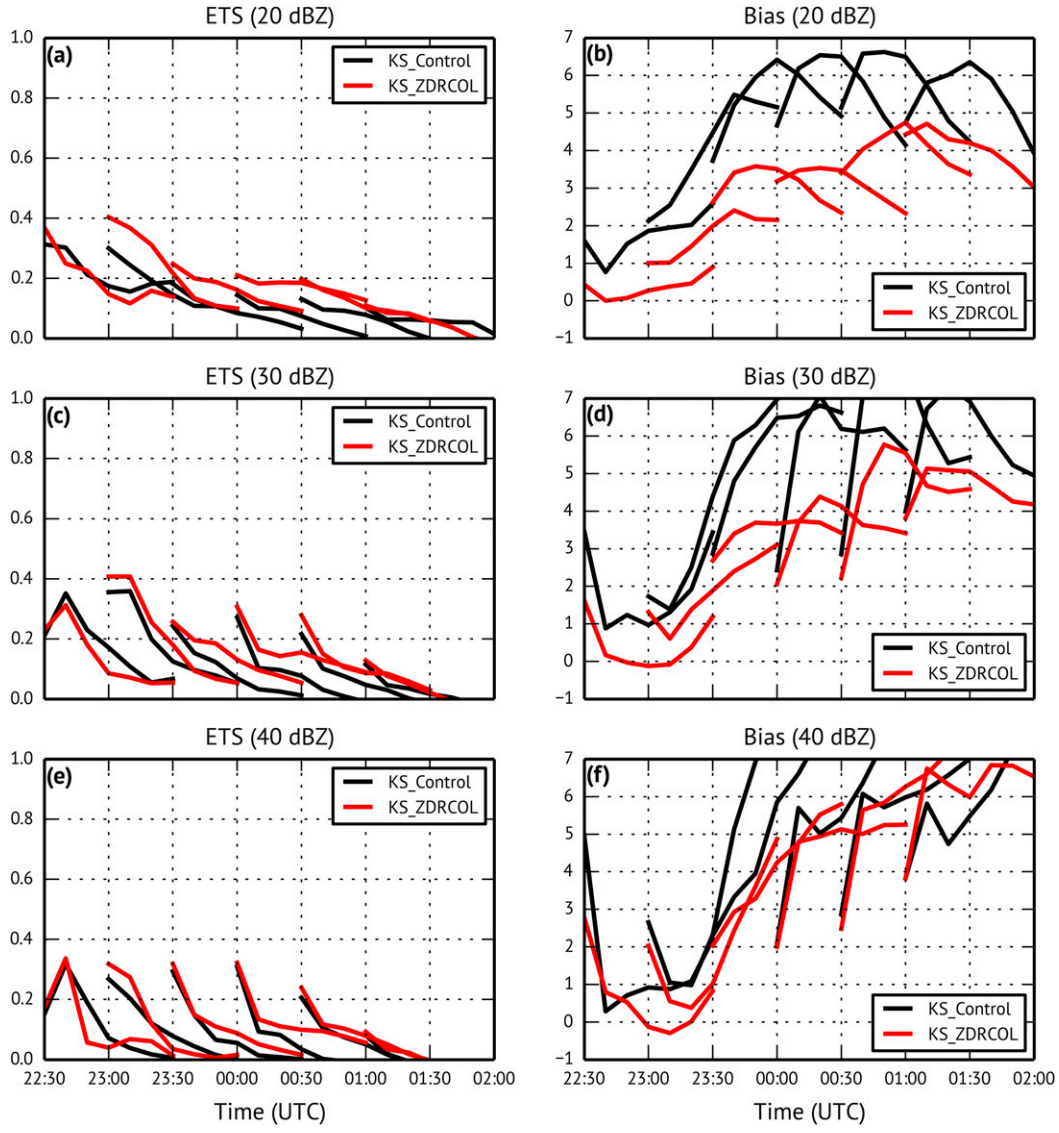

FIG. 14. As in Fig. 9, but for the KS case.

Overall scores are lower in the KS case, in part due to the challenging nature of the forecast and in part due to the aforementioned biases in Z (e.g., Figs. 14b,d,f) and the extensive forward-flank downdrafts, which generally exceed the biases seen for the OK case, particularly for later forecasts.

5. Summary and discussion

In this study, the potential for the assimilation of polarimetric radar data observations via a cloud analysis technique to aid in the spinup and forecast of convection in storm-scale models is examined. Differential reflectivity columns are ubiquitous features of deep moist convection that are coincident with updrafts and, thus, with areas of saturation and latent heat release. Based on this premise, a Z_{DR} column detection algorithm is developed to identify Z_{DR} columns and 1) insert positive temperature and moisture perturbations at these locations and 2) remove modest amounts of moisture outside of these locations where Z exceeds 10 dBZ. To evaluate this method, two cases are analyzed: the 19 May 2013 tornadic supercells in central Oklahoma and the 25 May 2016 tornadic supercell in north-central Kansas. For each case, two runs were performed to gauge the impact of these changes: a ''Control'' run using the original cloud analysis, and a ''ZDRCOL'' run using the newly modified cloud analysis that incorporates dual-polarization radar data.

The Z_{DR} column detection algorithm is shown to reliably identify Z_{DR} columns associated with convective updrafts, and notable qualitative and quantitative improvements in the analysis and forecasts of convection are seen in both cases. The analyzed updraft tracks are more coherent and consolidated with less spurious convection in the ZDRCOL runs than in the Control runs. The short-term forecasts show a reduction in forward speed and northward position bias of the main updrafts, an issue encountered in many storm-scale modeling experiments, with updraft helicity indicating better agreement with radar-derived rotation tracks in each case. The forecast Z fields also agree better with observations in the ZDRCOL runs compared to the Control runs, in turn leading to improved quantitative verification scores and reduced frequency bias.

These experiments represent a basic proof-of-concept investigation of the potential for assimilating Z_{DR} columns into storm-scale models and warrant further study. However, drawbacks to the method examined here exist that have yet to be addressed. First, while Z_{DR} columns are fairly ubiquitous in deep convection and generally collocated with updrafts, they can be masked by the presence of hail or tornadic debris (as discussed in Snyder et al. 2015) in the updraft, resulting in the intermittent appearance (or complete disappearance) of Z_{DR} columns; in some cases, Z_{DR} columns may not be observed in deep convection at all. Future work may examine the potential of using K_{DP} columns in a similar manner to alleviate these issues (van Lier-Walqui et al. 2016), although the use of K_{DP} columns bears its own shortcomings (e.g., poor estimation of K_{DP} in areas of limited precipitation). The use of Z_{DR} columns to aid spinup of precipitation in a NWP model may not be appropriate for weak convective storms and stratiform rain where Z_{DR} columns are ill defined or may not exist. Only two cases were analyzed in this study, with each being an archetypal case of very strong convection with good radar coverage and prominent Z_{DR} columns. The parameters both for detecting Z_{DR} columns and for applying moisture and temperature increments were subjectively determined and should undergo further refinement. Finally, only a single radar was assimilated for each case because of lingering uncertainty in the optimal methodology for merging polarimetric data from multiple radars, although work is ongoing (J. Krause 2017, personal communication) to implement the polarimetric compositing method developed in Homeyer (2014) and Homeyer and Kumjian (2015). The polarimetric version of the newly developed Storm Labeling in Three Dimensions (SL3D) algorithm (Starzec et al. 2017), which has demonstrated success in identifying convective updrafts using a combination of weak-echo regions, Z_{DR} columns, and K_{DP} columns, may also prove particularly useful going forward. It is likely that assimilating data from multiple radars would assist in the spinup and analysis of storms from radial velocity data beyond that examined in this work, as well as alleviate radar coverage concerns for detecting Z_{DR} columns.

While being a relatively simple and efficient method for assimilating Z, cloud analysis techniques may not be optimal owing to their inherent empirical relationships that can compromise initial adjustments in the model. As temperature and moisture increments appear to play large roles in aiding the spinup of observed storms in storm-scale models, future work will seek to explore the possibility of assimilating cloud analysis-derived temperature and moisture increments based on detected Z_{DR} columns as ''pseudo observations'' in a 3DVAR framework, similar to the work of Fierro et al. (2016) for lightning data assimilation. Using a variational framework to assimilate Z_{DR} columns would allow for a more balanced analysis/solution between the kinematic and thermodynamic fields and, hence, for a smoother cycling process.

Acknowledgments. The authors thank the three anonymous reviewers for their constructive feedback, as well as Keith Brewster and Elizabeth Smith for their helpful discussions and Alexandre Fierro for providing useful feedback about the manuscript. Funding was provided by NOAA/Office of Oceanic and Atmospheric Research under NOAA–University of Oklahoma Cooperative Agreement NA11OAR4320072, U.S. Department of Commerce. Additional funding was provided by the U.S. Department of Energy Atmospheric System Research Grant DE-SC0014295 and by NSF Grant AGS-1341878. The computing for this project was performed at the OU Supercomputing Center for Education and Research (OSCER) at the University of Oklahoma (OU).

REFERENCES

Aksoy, A., D. C. Dowell, and C. Snyder, 2009: A multicase comparative assessment of the ensemble Kalman filter for assimilation of radar observations. Part I: Storm-scale analyses. *Mon. Wea. Rev.*, **137**, 1805–1824, https://doi.org/10.1175/2008MWR2691.1.

Albers, S. C., J. A. McGinley, D. L. Birkenheuer, and J. R. Smart, 1996: The Local Analysis and Prediction System (LAPS): Analyses of clouds, precipitation, and temperature. *Wea. Forecasting*, **11**, 273–287, https://doi.org/10.1175/1520-0434(1996)011<0273:TLAAPS>2.0.CO;2.

Bodine, D. J., M. R. Kumjian, R. D. Palmer, P. L. Heinselman, and A. V. Ryzhkov, 2013: Tornado damage estimation using

polarimetric radar. *Wea. Forecasting*, **28**, 139–158, https://doi.org/10.1175/WAF-D-11-00158.1.

——, R. D. Palmer, and G. Zhang, 2014: Dual-wavelength polarimetric radar analyses of tornadic debris signatures. *J. Appl. Meteor. Climatol.*, **53**, 242–261, https://doi.org/10.1175/JAMC-D-13-0189.1.

Brewster, K. A., 2002: Recent advances in the diabatic initialization of a non-hydrostatic numerical model. *19th Conf. on Weather Analysis and Forecasting/15th Conf. on Numerical Weather Prediction/21st Conf. on Severe Local Storms*, San Antonio, TX, Amer. Meteor. Soc., J6.3, https://ams.confex.com/ams/SLS_WAF_NWP/techprogram/paper_47414.htm.

——, and D. R. Stratman, 2015: An updated high resolution hydrometeor analysis system using radar and other data. *27th Conf. on Weather Analysis and Forecasting/23rd Conf. on Numerical Weather Prediction*, Chicago, IL, Amer. Meteor. Soc., 31, https://ams.confex.com/ams/27WAF23NWP/webprogram/Paper273811.html.

——, M. Hu, M. Xue, and J. Gao, 2005: Efficient assimilation of radar data at high resolution for short range numerical weather prediction. *World Weather Research Program Symp. and Nowcasting and Very Short-Range Forecasting WSN05*, Toulouse, France, WMO World Weather Research Program, 3.06, http://twister.ou.edu/papers/BrewsterWWRP_Nowcasting.pdf.

Bringi, V. N., and V. Chandrasekar, 2001: *Polarimetric Doppler Weather Radar: Principles and Applications.* Cambridge University Press, 636 pp.

——, ——, N. Balakrishnan, and D. S. Zrnić, 1990: An examination of propagation effects in rainfall on radar measurements at microwave frequencies. *J. Atmos. Oceanic Technol.*, **7**, 829–840, https://doi.org/10.1175/1520-0426(1990)007<0829:AEOPEI>2.0.CO;2.

Brock, F. V., K. C. Crawford, R. L. Elliott, G. W. Cuperus, S. J. Stadler, H. L. Johnson, and M. D. Eilts, 1995: The Oklahoma mesonet: A technical overview. *J. Atmos. Oceanic Technol.*, **12**, 5–19, https://doi.org/10.1175/1520-0426(1995)012<0005:TOMATO>2.0.CO;2.

Carlin, J. T., A. V. Ryzhkov, J. C. Snyder, and A. Khain, 2016: Hydrometeor mixing ratio retrievals for storm-scale radar data assimilation: Utility of current relations and potential benefits of polarimetry. *Mon. Wea. Rev.*, **144**, 2981–3001, https://doi.org/10.1175/MWR-D-15-0423.1.

Caumont, O., V. Ducrocq, É. Wattrelot, G. Jaubert, and S. Pradier-Vabre, 2010: 1D+3DVar assimilation of radar reflectivity data: A proof of concept. *Tellus*, **62A**, 173–187, https://doi.org/10.1111/j.1600-0870.2009.00430.x.

Chang, S.-F., Y.-C. Liou, J. Sun, and S.-L. Tai, 2016: The implementation of the ice phase microphysical process into a four-dimensional Variational Doppler Radar Analysis System (VDRAS) and its impact on parameter retrieval and quantitative precipitation nowcasting. *J. Atmos. Sci.*, **73**, 1015–1038, https://doi.org/10.1175/JAS-D-15-0184.1.

Chou, M.-D., 1990: Parameterizations for the absorption of solar radiation by O_2 and CO_2 with application to climate studies. *J. Climate*, **3**, 209–217, https://doi.org/10.1175/1520-0442(1990)003<0209:PFTAOS>2.0.CO;2.

——, 1992: A solar radiation model for use in climate studies. *J. Atmos. Sci.*, **49**, 762–772, https://doi.org/10.1175/1520-0469(1992)049<0762:ASRMFU>2.0.CO;2.

Davolio, S., and A. Buzzi, 2004: A nudging scheme for the assimilation of precipitation data into a mesoscale model. *Wea. Forecasting*, **19**, 855–871, https://doi.org/10.1175/1520-0434(2004)019<0855:ANSFTA>2.0.CO;2.

Dawson, D. T., and M. Xue, 2006: Numerical forecasts of the 15–16 June 2002 southern plains mesoscale convective system: Impact of mesoscale data and cloud analysis. *Mon. Wea. Rev.*, **134**, 1607–1629, https://doi.org/10.1175/MWR3141.1.

——, L. J. Wicker, E. R. Mansell, Y. Jung, and M. Xue, 2013: Low-level polarimetric radar signatures in EnKF analyses and forecasts of the May 8, 2003 Oklahoma City tornadic supercell: Impact of multimoment microphysics and comparisons with observation. *Adv. Meteor.*, **2013**, 818394, https://doi.org/10.1155/2013/818394.

——, E. R. Mansell, Y. Jung, M. R. Kumjian, and M. Xue, 2014: Low-level Z_{DR} signatures in supercell forward flanks: The role of size sorting and melting hail. *J. Atmos. Sci.*, **71**, 276–299, https://doi.org/10.1175/JAS-D-13-0118.1.

——, M. Xue, J. A. Milbrandt, and A. Shapiro, 2015: Sensitivity of real-data simulations of the 3 May 1999 Oklahoma City tornadic supercell and associated tornadoes to multimoment microphysics. Part I: Storm- and tornado-scale numerical forecasts. *Mon. Wea. Rev.*, **143**, 2241–2265, https://doi.org/10.1175/MWR-D-14-00279.1.

Dowell, D. C., F. Zhang, L. J. Wicker, C. Snyder, and N. A. Crook, 2004: Wind and temperature retrievals in the 17 May 1981 Arcadia, Oklahoma, supercell: Ensemble Kalman filter experiments. *Mon. Wea. Rev.*, **132**, 1982–2005, https://doi.org/10.1175/1520-0493(2004)132<1982:WATRIT>2.0.CO;2.

——, L. J. Wicker, and C. Snyder, 2011: Ensemble Kalman filter assimilation of radar observations of the 8 May 2003 Oklahoma City supercell: Influences of reflectivity observations on storm-scale analyses. *Mon. Wea. Rev.*, **139**, 272–294, https://doi.org/10.1175/2010MWR3438.1.

Evensen, G., 1994: Sequential data assimilation with a nonlinear quasi-geostrophic model using Monte Carlo methods to forecast error statistics. *J. Geophys. Res.*, **99**, 10 143–10 162, https://doi.org/10.1029/94JC00572.

Fierro, A. O., E. R. Mansell, C. L. Ziegler, and D. R. MacGorman, 2012: Application of a lightning data assimilation technique in the WRF-ARW model at cloud-resolving scales for the tornado outbreak of 24 May 2011. *Mon. Wea. Rev.*, **140**, 2609–2627, https://doi.org/10.1175/MWR-D-11-00299.1.

——, J. Gao, C. L. Ziegler, E. R. Mansell, D. R. MacGorman, and S. R. Dembek, 2014: Evaluation of a cloud-scale lightning data assimilation technique and a 3DVAR method for the analysis and short-term forecast of the 29 June 2012 derecho event. *Mon. Wea. Rev.*, **142**, 183–202, https://doi.org/10.1175/MWR-D-13-00142.1.

——, A. Clark, E. R. Mansell, D. R. MacGorman, S. R. Dembek, and C. L. Ziegler, 2015: Impact of storm-scale lightning data assimilation on WRF-ARW precipitation forecasts during the 2013 warm season over the contiguous United States. *Mon. Wea. Rev.*, **143**, 757–777, https://doi.org/10.1175/MWR-D-14-00183.1.

——, J. Gao, C. L. Ziegler, K. M. Calhoun, E. R. Mansell, and D. R. MacGorman, 2016: Assimilation of flash extent data in the variational framework at convection-allowing scales: Proof-of-concept and evaluation for the short-term forecast of the 24 May 2011 tornado outbreak. *Mon. Wea. Rev.*, **144**, 4373–4393, https://doi.org/10.1175/MWR-D-16-0053.1.

Gao, J., and D. J. Stensrud, 2012: Assimilation of reflectivity data in a convective-scale, cycled 3DVAR framework with hydrometeor classification. *J. Atmos. Sci.*, **69**, 1054–1065, https://doi.org/10.1175/JAS-D-11-0162.1.

——, and ——, 2014: Some observing system simulation experiments with a hybrid 3DEnVAR system for storm-scale radar data assimilation. *Mon. Wea. Rev.*, **142**, 3326–3346, https://doi.org/10.1175/MWR-D-14-00025.1.

——, M. Xue, K. Brewster, and K. K. Droegemeier, 2004: A three-dimensional variational data analysis method with recursive filter for Doppler radars. *J. Atmos. Oceanic Technol.*, **21**, 457–469, https://doi.org/10.1175/1520-0426(2004)021<0457:ATVDAM>2.0.CO;2.

——, G. Ge, D. J. Stensrud, and M. Xue, 2009: The relative importance of assimilating radial velocity and reflectivity data. *23rd Conf. on Weather Analysis and Forecasting/19th Conf. on Numerical Weather Prediction*, Omaha, NE, Amer. Meteor. Soc., 8A.1, https://ams.confex.com/ams/23WAF19NWP/techprogram/paper_154286.htm.

——, M. Xue, and D. J. Stensrud, 2013: The development of a hybrid EnKF-3DVAR algorithm for storm-scale data assimilation. *Adv. Meteor.*, **2013**, 512656, https://doi.org/10.1155/2013/512656.

——, D. J. Stensrud, L. Wicker, M. Xue, and K. Zhao, 2014: Storm-scale radar data assimilation and high resolution NWP. *Adv. Meteor.*, **2014**, 213579, https://doi.org/10.1155/2014/213579.

——, C. Fu, D. J. Stensrud, and J. S. Kain, 2016: OSSEs for an ensemble 3DVAR data assimilation system with radar observations of convective storms. *J. Atmos. Sci.*, **73**, 2403–2426, https://doi.org/10.1175/JAS-D-15-0311.1.

Ge, G., J. Gao, and M. Xue, 2013: Impacts of assimilating measurements of different state variables with a simulated supercell storm and three-dimensional variational method. *Mon. Wea. Rev.*, **141**, 2759–2777, https://doi.org/10.1175/MWR-D-12-00193.1.

Gilbert, G. K., 1884: Finley's tornado predictions. *Amer. Meteor. J.*, **1**, 166–172.

Haines, P. A., J. K. Luers, and C. A. Cerbus, 1989: The role of the Smith–Feddes model in improving the forecasting of aircraft icing. *Third Conf. on the Aviation Weather System*, Anaheim, CA, Amer. Meteor. Soc., 258–263.

Hall, M. P. M., J. W. F. Goddard, and S. M. Cherry, 1984: Identification of hydrometeors and other targets by dual-polarization radar. *Radio Sci.*, **19**, 132–140, https://doi.org/10.1029/RS019i001p00132.

Heinselman, P. L., and A. V. Ryzhkov, 2006: Validation of polarimetric hail detection. *Wea. Forecasting*, **21**, 839–850, https://doi.org/10.1175/WAF956.1.

Homeyer, C. R., 2014: Formation of the enhanced-V infrared cloud-top feature from high-resolution three-dimensional radar observations. *J. Atmos. Sci.*, **71**, 332–348, https://doi.org/10.1175/JAS-D-13-079.1.

——, and M. R. Kumjian, 2015: Microphysical characteristics of overshooting convection from polarimetric radar observations. *J. Atmos. Sci.*, **72**, 870–891, https://doi.org/10.1175/JAS-D-13-0388.1.

Hu, M., and M. Xue, 2007: Impact of configurations of rapid intermittent assimilation of WSR-88D radar data for the 8 May 2003 Oklahoma City tornadic thunderstorm case. *Mon. Wea. Rev.*, **135**, 507–525, https://doi.org/10.1175/MWR3313.1.

——, ——, and K. Brewster, 2006a: 3DVAR and cloud analysis with WSR-88D level-II data for the prediction of the Fort Worth, Texas, tornadic thunderstorms. Part I: Cloud analysis and its impact. *Mon. Wea. Rev.*, **134**, 675–698, https://doi.org/10.1175/MWR3092.1.

——, ——, J. Gao, and K. Brewster, 2006b: 3DVAR and cloud analysis with WSR-88D level-II data for the prediction of the Fort Worth, Texas, tornadic thunderstorms. Part II: Impact of radial velocity analysis via 3DVAR. *Mon. Wea. Rev.*, **134**, 699–721, https://doi.org/10.1175/MWR3093.1.

Illingworth, A. J., J. W. F. Goddard, and S. M. Cherry, 1987: Polarization radar studies of precipitation development in convective storms. *Quart. J. Roy. Meteor. Soc.*, **113**, 469–489, https://doi.org/10.1002/qj.49711347604.

Johnson, M., Y. Jung, D. Dawson, and M. Xue, 2016: Comparison of simulated polarimetric signatures in idealized supercell storms using two-moment bulk microphysics schemes in WRF. *Mon. Wea. Rev.*, **144**, 971–996, https://doi.org/10.1175/MWR-D-15-0233.1.

Jones, C. D., and B. Macpherson, 1997: A latent heat nudging scheme for the assimilation of precipitation data into an operational mesoscale model. *Meteor. Appl.*, **4**, 269–277, https://doi.org/10.1017/S1350482797000522.

Jung, Y., G. Zhang, and M. Xue, 2008a: Assimilation of simulated polarimetric radar data for a convective storm using the ensemble Kalman filter. Part I: Observation operators for reflectivity and polarimetric variables. *Mon. Wea. Rev.*, **136**, 2228–2245, https://doi.org/10.1175/2007MWR2083.1.

——, ——, ——, and J. M. Straka, 2008b: Assimilation of simulated polarimetric radar data for a convective storm using the ensemble Kalman filter. Part II: Impact of polarimetric data on storm analysis. *Mon. Wea. Rev.*, **136**, 2246–2260, https://doi.org/10.1175/2007MWR2288.1.

——, M. Xue, and G. Zhang, 2010a: Simulations of polarimetric radar signatures of a supercell storm using a two-moment bulk microphysics scheme. *J. Appl. Meteor. Climatol.*, **49**, 146–163, https://doi.org/10.1175/2009JAMC2178.1.

——, ——, and ——, 2010b: Simultaneous estimation of microphysical parameters and the atmospheric state using simulated polarimetric radar data and an ensemble Kalman filter in the presence of an observation operator error. *Mon. Wea. Rev.*, **138**, 539–562, https://doi.org/10.1175/2009MWR2748.1.

——, ——, and M. Tong, 2012: Ensemble Kalman filter analyses of the 29–30 May 2004 Oklahoma tornadic thunderstorm using one- and two-moment bulk microphysics schemes, with verification against polarimetric radar data. *Mon. Wea. Rev.*, **140**, 1457–1475, https://doi.org/10.1175/MWR-D-11-00032.1.

Kain, J. S., and Coauthors, 2008: Some practical considerations regarding horizontal resolution in the first generation of operational convection-allowing NWP. *Wea. Forecasting*, **23**, 931–952, https://doi.org/10.1175/WAF2007106.1.

Khain, A., A. Pokrovsky, M. Pinsky, A. Seifert, and V. Phillips, 2004: Simulation of effects of atmospheric aerosols on deep turbulent convective clouds using a spectral microphysics mixed-phase cumulus cloud model. Part I: Model description and possible applications. *J. Atmos. Sci.*, **61**, 2963–2982, https://doi.org/10.1175/JAS-3350.1.

Knight, C. A., 2006: Very early formation of big, liquid drops revealed by Z_{DR} in continental cumulus. *J. Atmos. Sci.*, **63**, 1939–1953, https://doi.org/10.1175/JAS3721.1.

Koch, S. E., A. Aksakal, and J. T. McQueen, 1997: The influence of mesoscale humidity and evapotranspiration fields on a model forecast of a cold-frontal squall line. *Mon. Wea. Rev.*, **125**, 384–409, https://doi.org/10.1175/1520-0493(1997)125<0384:TIOMHA>2.0.CO;2.

Korsholm, U., C. Petersen, B. H. Sass, N. W. Nielsen, D. G. Jensen, B. T. Olsen, R. Gill, and H. Vedel, 2015: A new approach for assimilation of 2D radar precipitation in a high-resolution NWP model. *Meteor. Appl.*, **22**, 48–59, https://doi.org/10.1002/met.1466.

Kumjian, M. R., 2013a: Principles and applications of dual-polarization weather radar. Part I: Description of the polarimetric radar variables. *J. Oper. Meteor.*, **1**, 226–242, https://doi.org/10.15191/nwajom.2013.0119.

——, 2013b: Principles and applications of dual-polarization weather radar. Part II: Warm- and cold-season applications. *J. Oper. Meteor.*, **1**, 243–264, https://doi.org/10.15191/nwajom.2013.0120.

——, 2013c: Principles and applications of dual-polarization weather radar. Part III: Artifacts. *J. Oper. Meteor.*, **1**, 265–274, https://doi.org/10.15191/nwajom.2013.0121.

——, and A. V. Ryzhkov, 2012: The impact of size sorting on the polarimetric radar variables. *J. Atmos. Sci.*, **69**, 2042–2060, https://doi.org/10.1175/JAS-D-11-0125.1.

——, A. P. Khain, N. Benmoshe, E. Ilotoviz, A. V. Ryzhkov, and V. T. Phillips, 2014: The anatomy and physics of Z_{DR} columns: Investigating a polarimetric radar signature with a spectral bin microphysical model. *J. Appl. Meteor. Climatol.*, **53**, 1820–1843, https://doi.org/10.1175/JAMC-D-13-0354.1.

Leuenberger, D., and A. Rossa, 2007: Revisiting the latent heat nudging scheme for the rainfall assimilation of a simulated convective storm. *Meteor. Atmos. Phys.*, **98**, 195–215, https://doi.org/10.1007/s00703-007-0260-9.

Li, X., and J. Mecikalski, 2010: Assimilation of the dual-polarization Doppler radar data for a convective storm with a warm-rain radar forward operator. *J. Geophys. Res.*, **115**, D16208, https://doi.org/10.1029/2009JD013666.

——, and ——, 2012: Impact of the dual-polarization Doppler radar data on two convective storms with a warm-rain radar forward operator. *Mon. Wea. Rev.*, **140**, 2147–2167, https://doi.org/10.1175/MWR-D-11-00090.1.

Lin, Y.-L., R. D. Farley, and H. D. Orville, 1983: Bulk parameterization of the snow field in a cloud model. *J. Climate Appl. Meteor.*, **22**, 1065–1092, https://doi.org/10.1175/1520-0450(1983)022<1065:BPOTSF>2.0.CO;2.

Macpherson, B., 2001: Operational experience with assimilation of rainfall data in the Met Office Mesoscale model. *Meteor. Atmos. Phys.*, **76**, 3–8, https://doi.org/10.1007/s007030170035.

Marchand, M. R., and H. E. Fuelberg, 2014: Assimilation of lightning data using a nudging method involving low-level warming. *Mon. Wea. Rev.*, **142**, 4850–4871, https://doi.org/10.1175/MWR-D-14-00076.1.

Milbrandt, J., and M. Yau, 2005a: A multimoment bulk microphysics parameterization. Part I: Analysis of the role of the spectral shape parameter. *J. Atmos. Sci.*, **62**, 3051–3064, https://doi.org/10.1175/JAS3534.1.

——, and ——, 2005b: A multimoment bulk microphysics parameterization. Part II: A proposed three-moment closure and scheme description. *J. Atmos. Sci.*, **62**, 3065–3081, https://doi.org/10.1175/JAS3535.1.

Noilhan, J., and S. Planton, 1989: A simple parameterization of land surface processes for meteorological models. *Mon. Wea. Rev.*, **117**, 536–549, https://doi.org/10.1175/1520-0493(1989)117<0536:ASPOLS>2.0.CO;2.

Noppel, H., U. Blahak, A. Seifert, and K. D. Beheng, 2010: Simulations of a hailstorm and the impact of CCN using an advanced two-moment cloud microphysical scheme. *Atmos. Res.*, **96**, 286–301, https://doi.org/10.1016/j.atmosres.2009.09.008.

NWS, 2017a: The tornado outbreak of May 19, 2013. NWS Forecast Office, Norman, OK, accessed 6 February 2017, http://www.weather.gov/oun/events-20130519.

——, 2017b: Wednesday, May 25th, 2016: Long track tornado hits north central Kansas. NWS Forecast Office, Topeka, KS, accessed 6 February 2017, http://www.weather.gov/top/LongTrackTornadoHitsNorthCentralKS.

Pan, Y., M. Xue, and G. Ge, 2016: Incorporating diagnosed intercept parameters and the graupel category within the ARPS cloud analysis system for the initialization of double-moment microphysics: Testing with a squall line over South China. *Mon. Wea. Rev.*, **144**, 371–392, https://doi.org/10.1175/MWR-D-15-0008.1.

Park, H., A. V. Ryzhkov, D. S. Zrnić, and K.-E. Kim, 2009: The hydrometeor classification algorithm for the polarimetric WSR-88D: Description and application to an MCS. *Wea. Forecasting*, **24**, 730–748, https://doi.org/10.1175/2008WAF2222205.1.

Pfeifer, M., G. C. Craig, M. Hagen, and C. Keil, 2008: A polarimetric radar forward operator for model evaluation. *J. Appl. Meteor. Climatol.*, **47**, 3202–3220, https://doi.org/10.1175/2008JAMC1793.1.

Picca, J. C., M. Kumjian, and A. Ryzhkov, 2010: Z_{DR} columns as a predictive tool for hail growth and storm evolution. *25th Conf. on Severe Local Storms*, Denver, CO, Amer. Meteor. Soc., 11.3, https://ams.confex.com/ams/25SLS/techprogram/paper_175750.htm.

——, D. M. Kingfield, and A. V. Ryzhkov, 2017: Utilizing a polarimetric size sorting signature to develop a convective nowcasting algorithm. *18th Conf. on Aviation, Range, and Aerospace Meteorology*, Seattle, WA, Amer. Meteor. Soc., 14.5, https://ams.confex.com/ams/97Annual/webprogram/Paper308684.html.

Potvin, C. K., L. J. Wicker, M. M. French, and D. D. Burgess, 2014: Warn-on-Forecast sensitivity experiments with the 19 May 2013 Norman-Shawnee, OK, tornadic supercell. *27th Conf. on Severe Local Storms*, Madison, WI, Amer. Meteor. Soc., 8A.3, https://ams.confex.com/ams/27SLS/webprogram/Paper255559.html.

Putnam, B. J., M. Xue, Y. Jung, N. A. Snook, and G. Zhang, 2014: The analysis and prediction of microphysical states and polarimetric radar variables in a mesoscale convective system using double-moment microphysics, multinetwork radar data, and the ensemble Kalman filter. *Mon. Wea. Rev.*, **142**, 141–162, https://doi.org/10.1175/MWR-D-13-00042.1.

Rogers, R. F., J. M. Fritsch, and W. C. Lambert, 2000: A simple technique for using radar data in the dynamic initialization of a mesoscale model. *Mon. Wea. Rev.*, **128**, 2560–2574, https://doi.org/10.1175/1520-0493(2000)128<2560:ASTFUR>2.0.CO;2.

Ryzhkov, A. V., V. B. Zhuravlyov, and N. A. Rybakova, 1994: Preliminary results of X-band polarization radar studies of clouds and precipitation. *J. Atmos. Oceanic Technol.*, **11**, 132–139, https://doi.org/10.1175/1520-0426(1994)011<0132:PROXBP>2.0.CO;2.

——, S. E. Giangrande, and T. J. Schuur, 2005a: Rainfall estimation with a polarimetric prototype of WSR-88D. *J. Appl. Meteor.*, **44**, 502–515, https://doi.org/10.1175/JAM2213.1.

——, T. J. Schuur, D. W. Burgess, and D. S. Zrnić, 2005b: Polarimetric tornado detection. *J. Appl. Meteor.*, **44**, 557–570, https://doi.org/10.1175/JAM2235.1.

——, M. Pinsky, A. Pokrovsky, and A. Khain, 2011: Polarimetric radar observation operator for a cloud model with spectral microphysics. *J. Appl. Meteor. Climatol.*, **50**, 873–894, https://doi.org/10.1175/2010JAMC2363.1.

——, M. R. Kumjian, S. M. Ganson, and A. P. Khain, 2013a: Polarimetric radar characteristics of melting hail. Part I: Theoretical simulations using spectral microphysical modeling. *J. Appl. Meteor. Climatol.*, **52**, 2849–2869, https://doi.org/10.1175/JAMC-D-13-073.1.

——, ——, ——, and P. Zhang, 2013b: Polarimetric radar characteristics of melting hail. Part II: Practical implications. *J. Appl. Meteor. Climatol.*, **52**, 2871–2886, https://doi.org/10.1175/JAMC-D-13-074.1.

Schenkman, A. D., 2012: Exploring tornadogenesis with high-resolution simulations initialized with real data. Ph.D. dissertation, University of Oklahoma, 161 pp.

——, M. Xue, A. Shapiro, K. Brewster, and J. Gao, 2011: The analysis and prediction of the 8–9 May 2007 Oklahoma tornadic mesoscale convective system by assimilating WSR-88D and CASA radar data using 3DVAR. *Mon. Wea. Rev.*, **139**, 224–246, https://doi.org/10.1175/2010MWR3336.1.

Schultz, C. J., and Coauthors, 2012a: Dual-polarization tornadic debris signatures. Part I: Examples and utility in an operational setting. *Electron. J. Oper. Meteor.*, **13**, 120–137, http://nwafiles.nwas.org/ej/pdf/2012-EJ9.pdf.

——, and Coauthors, 2012b: Dual-polarization tornadic debris signatures. Part II: Comparisons and caveats. *Electron. J. Oper. Meteor.*, **13**, 138–150, http://nwafiles.nwas.org/ej/pdf/2012-EJ10.pdf.

Smith, P. L., C. G. Myers, and H. D. Orville, 1975: Radar reflectivity factor calculations in numerical cloud models using bulk parameterization of precipitation. *J. Appl. Meteor.*, **14**, 1156–1165, https://doi.org/10.1175/1520-0450(1975)014<1156:RRFCIN>2.0.CO;2.

Smith, T. M., and K. M. Elmore, 2004: The use of radial velocity derivatives to diagnose rotation and divergence. *11th Conf. on Aviation, Range, and Aerospace*, Hyannis, MA, Amer. Meteor. Soc., P5.6, https://ams.confex.com/ams/pdfpapers/81827.pdf.

——, and Coauthors, 2016: Multi-Radar Multi-Sensor (MRMS) severe weather and aviation products: Initial operating capabilities. *Bull. Amer. Meteor. Soc.*, **97**, 1617–1630, https://doi.org/10.1175/BAMS-D-14-00173.1.

Snook, N., M. Xue, and Y. Jung, 2011: Analysis of a tornadic mesoscale convective vortex based on ensemble Kalman filter assimilation of CASA X-band and WSR-88D radar data. *Mon. Wea. Rev.*, **139**, 3446–3468, https://doi.org/10.1175/MWR-D-10-05053.1.

——, ——, and ——, 2012: Ensemble probabilistic forecasts of a tornadic mesoscale convective system from ensemble Kalman filter analyses using WSR-88D and CASA radar data. *Mon. Wea. Rev.*, **140**, 2126–2146, https://doi.org/10.1175/MWR-D-11-00117.1.

Snyder, J. C., and A. V. Ryzhkov, 2015: Automated detection of polarimetric tornadic debris signatures using a hydrometeor classification algorithm. *J. Appl. Meteor. Climatol.*, **54**, 1861–1870, https://doi.org/10.1175/JAMC-D-15-0138.1.

——, H. B. Bluestein, G. Zhang, and S. J. Frasier, 2010: Attenuation correction and hydrometeor classification of high-resolution, X-band, dual-polarized mobile radar measurements in severe convective storms. *J. Atmos. Oceanic Technol.*, **27**, 1979–2001, https://doi.org/10.1175/2010JTECHA1356.1.

——, A. V. Ryzhkov, M. R. Kumjian, A. P. Khain, and J. Picca, 2015: A Z_{DR} column detection algorithm to examine convective storm updrafts. *Wea. Forecasting*, **30**, 1819–1844, https://doi.org/10.1175/WAF-D-15-0068.1.

——, H. B. Bluestein, D. T. Dawson, and Y. Jung, 2017a: Simulations of polarimetric, X-band radar signatures in supercells. Part I: Description of experiment and simulated ρ_{hv} rings. *J. Appl. Meteor. Climatol.*, **56**, 1977–1999, https://doi.org/10.1175/JAMC-D-16-0138.1.

——, ——, ——, and ——, 2017b: Simulations of polarimetric, X-band radar signatures in supercells. Part II: Z_{DR} columns and rings and K_{DP} columns. *J. Appl. Meteor. Climatol.*, **56**, 2001–2026, https://doi.org/10.1175/JAMC-D-16-0139.1.

Souto, M. J., C. F. Balseiro, V. Pérez-Muñuzuri, M. Xue, and K. Brewster, 2003: Impact of cloud analysis on numerical weather prediction in the Galician region of Spain. *J. Appl. Meteor.*, **42**, 129–140, https://doi.org/10.1175/1520-0450(2003)042<0129:IOCAON>2.0.CO;2.

Starzec, M., C. R. Homeyer, and G. L. Mullendore, 2017: Storm Labeling in Three Dimensions (SLD3): A volumetric radar echo and dual-polarization updraft classification algorithm. *Mon. Wea. Rev.*, **145**, 1127–1145, https://doi.org/10.1175/MWR-D-16-0089.1.

Stensrud, D. J., and Coauthors, 2009: Convective-scale Warn-on-Forecast system: A vision for 2020. *Bull. Amer. Meteor. Soc.*, **90**, 1487–1499, https://doi.org/10.1175/2009BAMS2795.1.

——, and Coauthors, 2013: Progress and challenges with Warn-on-Forecast. *Atmos. Res.*, **123**, 2–16, https://doi.org/10.1016/j.atmosres.2012.04.004.

Stephan, K., S. Klink, and C. Schraff, 2008: Assimilation of radar-derived rain rates into the convective-scale model COSMO-DE at DWD. *Quart. J. Roy. Meteor. Soc.*, **134**, 1315–1326, https://doi.org/10.1002/qj.269.

Stratman, D. R., and K. A. Brewster, 2015: Verification of 24 May 2011 simulated mesocyclones using various microphysics schemes at 1-km grid resolution. *27th Conf. on Weather Analysis and Forecasting/23rd Conf. on Numerical Weather Prediction*, Chicago, IL, Amer. Meteor. Soc., 13A.6, https://ams.confex.com/ams/27WAF23NWP/webprogram/Manuscript/Paper273795/stratman_wafnwp_2015.pdf.

Sun, J., 2005: Initialization and numerical forecasting of a supercell storm observed during STEPS. *Mon. Wea. Rev.*, **133**, 793–813, https://doi.org/10.1175/MWR2887.1.

——, and A. N. Crook, 1997: Dynamical and microphysical retrieval from Doppler radar observations using a cloud model and its adjoint. Part I: Model development and simulated data experiments. *J. Atmos. Sci.*, **54**, 1642–1661, https://doi.org/10.1175/1520-0469(1997)054<1642:DAMRFD>2.0.CO;2.

——, and ——, 1998: Dynamical and microphysical retrieval from Doppler radar observations using a cloud model and its adjoint. Part II: Retrieval experiments of an observed Florida convective storm. *J. Atmos. Sci.*, **55**, 835–852, https://doi.org/10.1175/1520-0469(1998)055<0835:DAMRFD>2.0.CO;2.

——, and Y. Zhang, 2008: Analysis and prediction of a squall line observed during IHOP using multiple WSR-88D observations. *Mon. Wea. Rev.*, **136**, 2364–2388, https://doi.org/10.1175/2007MWR2205.1.

Sun, W.-Y., and C.-Z. Chang, 1986: Diffusion model for a convective layer. Part I: Numerical simulation of convective boundary layer. *J. Climate Appl. Meteor.*, **25**, 1445–1453, https://doi.org/10.1175/1520-0450(1986)025<1445:DMFACL>2.0.CO;2.

Tabary, P., A.-A. Boumahmoud, H. Andrieu, R. J. Thompson, A. J. Illingworth, E. Le Bouar, and J. Testud, 2011: Evaluation of two ''integrated'' polarimetric quantitative precipitation estimation (QPE) algorithms at C-band. *J. Hydrol.*, **405**, 248–260, https://doi.org/10.1016/j.jhydrol.2011.05.021.

Testud, J., Le Bouar, E., E. Obligis, and M. Ali-Mehenni, 2000: The rain profiling algorithm applied to polarimetric weather radar. *J. Atmos. Oceanic Technol.*, **17**, 332–356, https://doi.org/10.1175/1520-0426(2000)017<0332:TRPAAT>2.0.CO;2.

Tong, C.-C., 2015: Limitations and potential of complex cloud analysis and its improvement for radar reflectivity data assimilation using OSSEs. Ph.D. dissertation, University of Oklahoma, 192 pp., https://shareok.org/handle/11244/25756.

Tong, M., and M. Xue, 2005: Ensemble Kalman filter assimilation of Doppler radar data with a compressible nonhydrostatic model: OSS experiments. *Mon. Wea. Rev.*, **133**, 1789–1807, https://doi.org/10.1175/MWR2898.1.

Tuttle, J. D., V. N. Bringi, H. D. Orville, and F. J. Kopp, 1989: Preliminary results of X-band polarization radar studies of

clouds and precipitation. *J. Atmos. Sci.*, **46**, 601–620, https://doi.org/10.1175/1520-0469(1989)046<0601:MRSOAM>2.0.CO;2.

Van Den Broeke, M. S., and S. T. Jauernic, 2014: Spatial and temporal characteristics of polarimetric tornadic debris signatures. *J. Appl. Meteor. Climatol.*, **53**, 2217–2231, https://doi.org/10.1175/JAMC-D-14-0094.1.

van Lier-Walqui, M., and Coauthors, 2016: On polarimetric radar signatures of deep convection for model evaluation: Columns of specific differential phase observed during MC3E. *Mon. Wea. Rev.*, **144**, 737–758, https://doi.org/10.1175/MWR-D-15-0100.1.

Wainwright, C. E., D. T. Dawson, M. Xue, and G. Zhang, 2014: Diagnosing the intercept parameters of the exponential drop size distributions in a single-moment microphysics scheme and impact on supercell storm simulations. *J. Appl. Meteor. Climatol.*, **53**, 2072–2090, https://doi.org/10.1175/JAMC-D-13-0251.1.

Wang, H., J. Sun, S. Fan, and X.-Y. Huang, 2013a: Indirect assimilation of radar reflectivity with WRF 3D-Var and its impact on prediction of four summertime convective events. *J. Appl. Meteor. Climatol.*, **52**, 889–902, https://doi.org/10.1175/JAMC-D-12-0120.1.

——, ——, X. Zhang, X.-Y. Huang, and T. Auligné, 2013b: Radar data assimilation with WRF 4D-Var. Part I: System development and preliminary testing. *Mon. Wea. Rev.*, **141**, 2224–2244, https://doi.org/10.1175/MWR-D-12-00168.1.

Wang, X., D. M. Barker, C. Snyder, and T. M. Hamill, 2008a: A hybrid ETKF–3DVAR data assimilation scheme for the WRF Model. Part I: Observing system simulation experiment. *Mon. Wea. Rev.*, **136**, 5116–5131, https://doi.org/10.1175/2008MWR2444.1.

——, ——, ——, and ——, 2008b: A hybrid ETKF–3DVAR data assimilation scheme for the WRF Model. Part II: Real observation experiments. *Mon. Wea. Rev.*, **136**, 5132–5147, https://doi.org/10.1175/2008MWR2445.1.

Weygandt, S. S., A. Shapiro, and K. K. Droegemeier, 2002: Retrieval of model initial fields from single-Doppler observations of a supercell thunderstorm. Part II: Thermodynamic retrieval and numerical prediction. *Mon. Wea. Rev.*, **130**, 454–476, https://doi.org/10.1175/1520-0493(2002)130<0454:ROMIFF>2.0.CO;2.

Wheatley, D. M., K. H. Knopfmeier, T. A. Jones, and G. J. Creager, 2015: Storm-scale data assimilation and ensemble forecasting with the NSSL experimental Warn-on-Forecast system. Part I: Radar data experiments. *Wea. Forecasting*, **30**, 1795–1817, https://doi.org/10.1175/WAF-D-15-0043.1.

Wu, B., J. Verlinde, and J. Sun, 2000: Dynamical and microphysical retrievals from Doppler radar observations of a deep convective cloud. *J. Atmos. Sci.*, **57**, 262–283, https://doi.org/10.1175/1520-0469(2000)057<0262:DAMRFD>2.0.CO;2.

Xiao, Q., Y.-H. Kuo, J. Sun, W.-C. Lee, E. Lim, Y.-R. Guo, and D. M. Barker, 2005: Assimilation of Doppler radar observations with a regional 3DVAR system: Impact of Doppler velocities on forecasts of a heavy rainfall case. *J. Appl. Meteor.*, **44**, 768–788, https://doi.org/10.1175/JAM2248.1.

——, ——, ——, ——, D. M. Barker, and E. Lim, 2007: An approach of radar reflectivity data assimilation and its assessment with the inland QPF of Typhoon Rusa (2002) at landfall. *J. Appl. Meteor. Climatol.*, **46**, 14–22, https://doi.org/10.1175/JAM2439.1.

Xue, M., K. K. Droegemeier, and V. Wong, 2000: The Advanced Regional Prediction System (ARPS)—A multi-scale nonhydrostatic atmospheric simulation and prediction tool. Part I: Model dynamics and verification. *Meteor. Atmos. Phys.*, **75**, 161–193, https://doi.org/10.1007/s007030070003.

——, ——, and ——, 2001: The Advanced Regional Prediction System (ARPS)—A multi-scale nonhydrostatic atmospheric simulation and prediction tool. Part II: Model physics and applications. *Meteor. Atmos. Phys.*, **76**, 143–165, https://doi.org/10.1007/s007030170027.

——, D. Wang, J. Gao, K. Brewster, and K. K. Droegemeier, 2003: The Advanced Regional Prediction System (ARPS), storm-scale numerical weather prediction and data assimilation. *Meteor. Atmos. Phys.*, **82**, 139–170, https://doi.org/10.1007/s00703-001-0595-6.

——, M. Tong, and K. K. Droegemeier, 2006: An OSSE framework based on the ensemble square root Kalman filter for evaluating the impact of data from radar networks on thunderstorm analysis and forecasting. *J. Atmos. Oceanic Technol.*, **23**, 46–66, https://doi.org/10.1175/JTECH1835.1.

——, M. Hu, and A. D. Schenkman, 2014: Numerical prediction of the 8 May 2003 Oklahoma City tornadic supercell and embedded tornado using ARPS with the assimilation of WSR-88D data. *Wea. Forecasting*, **29**, 39–62, https://doi.org/10.1175/WAF-D-13-00029.1.

Yokota, S., H. Seko, M. Kunii, H. Yamauchi, and H. Niino, 2016: The tornadic supercell on the Kanto Plain on 6 May 2012: Polarimetric radar and surface data assimilation with EnKF and ensemble-based sensitivity analysis. *Mon. Wea. Rev.*, **144**, 3133–3157, https://doi.org/10.1175/MWR-D-15-0365.1.

Yussouf, N., and D. J. Stensrud, 2010: Impact of phased-array radar observations over a short assimilation period: Observing system simulation experiments using an ensemble Kalman filter. *Mon. Wea. Rev.*, **138**, 517–538, https://doi.org/10.1175/2009MWR2925.1.

——, E. R. Mansell, L. J. Wicker, D. M. Wheatley, and D. J. Stensrud, 2013: The ensemble Kalman filter analyses and forecasts of the 8 May 2003 Oklahoma City tornadic supercell storm using single- and double-moment microphysics schemes. *Mon. Wea. Rev.*, **141**, 3388–3412, https://doi.org/10.1175/MWR-D-12-00237.1.

Zhang, G., M. Xue, Q. Cao, and D. Dawson, 2008: Diagnosing the intercept parameter for exponential raindrop size distribution based on video disdrometer observations: Model development. *J. Appl. Meteor. Climatol.*, **47**, 2983–2992, https://doi.org/10.1175/2008JAMC1876.1.

Zhang, J., 1999: Moisture and diabatic initialization based on radar and satellite observation. Ph.D. dissertation, University of Oklahoma, 194 pp.

——, F. Carr, and K. Brewster, 1998: ADAS cloud analysis. Preprints, *12th Conf. on Numerical Weather Prediction*, Phoenix, AZ, Amer. Meteor. Soc., 185–188.

Zhao, K., and M. Xue, 2009: Assimilation of coastal Doppler radar data with the ARPS 3DVAR and cloud analysis for the prediction of Hurricane Ike (2008). *Geophys. Res. Lett.*, **36**, L12803, https://doi.org/10.1029/2009GL038658.

Zhuang, Z., N. Yussouf, and J. Gao, 2016: Analyses and forecasts of a tornadic supercell outbreak using a 3DVAR system ensemble. *Adv. Atmos. Sci.*, **33**, 544–558, https://doi.org/10.1007/s00376-015-5072-0.

Zrnić, D. S., and A. V. Ryzhkov, 1996: Advantages of rain measurements using specific differential phase. *J. Atmos. Oceanic Technol.*, **13**, 454–464, https://doi.org/10.1175/1520-0426(1996)013<0454:AORMUS>2.0.CO;2.

——, and ——, 1999: Polarimetry for weather surveillance radars. *Bull. Amer. Meteor. Soc.*, **80**, 389–406, https://doi.org/10.1175/1520-0477(1999)080<0389:PFWSR>2.0.CO;2.